Micro Shear Bands: Precursor for Strain Localization in Sheared Granular Materials

Siavash Amirrahmat[1]; Andrew M. Druckrey[2]; Khalid A. Alshibli, M.ASCE[3]; and Riyadh I. Al-Raoush[4]

Abstract: Recent studies have shown that detection of the onset and evolution of micro shear bands (MSBs) in granular materials can be improved using measurements of the kinematic behavior of particles. Different methods such as the discrete-element method (DEM) or three-dimensional (3D) imaging techniques have been used to measure the kinematics of individual particles within triaxial specimens. However, conventional kinematic techniques that use particle translation and/or rotation cannot detect the onset and growth of MSBs during the hardening phase of axisymmetric triaxial experiments. In order to expose the localized shearing and particle-scale behavior of triaxial specimens, a relative particle translation gradient (RPTG) concept is used to detect and expose the onset of strain localization before the peak principal stress ratio (PSR). RPTG measurements for four different granular materials are reported in this paper. The RPTG concept is used to expose the onset of MSBs during the hardening phase of the experiments. In addition, the contact number of individual particles is quantified and discussed in relation to particle rotation to investigate a particle-scale relationship between particle contacts and rotation. The effects of density, confining pressure, and particle shape on contact number are examined. **DOI: 10.1061/(ASCE)GT.1943-5606.0001989.**

Author keywords: Particle kinematic behavior; Strain localization; Shear bands; Triaxial compression; Contact number.

Introduction

Soils may fail via diffuse bifurcation or as a result of the localization of plastic shear strains into zones of intensive shearing known as shear bands. The literature is rich with studies that investigated the mechanism of strain localization in granular materials; these studies can be broadly classified as continuum or microscale-discrete approaches. Common methods such as the discrete-element method (DEM) (Jiang et al. 2010; Kuhn and Bagi 2004; Oda and Iwashita 2000; Oda et al. 1997), two-dimensional (2D) or three-dimensional (3D) digital image correlation (DIC) techniques [digital image correlation and volumetric-digital image correlation (V-DIC)] (Hall et al. 2010a; Rechenmacher and Finno 2003), computed tomography (CT) or synchrotron microcomputed tomography (SMT), and numerical and analytical methods (Alshibli et al. 2006; Huang et al. 2002; Oda et al. 1997; Walker et al. 2013) have been used to study the stress and strain fields and the onset and evolution of shear bands. Studying particle kinematics offers valuable insights into the failure mode of granular materials in terms of particle translation and rotation.

The quantification of particle-scale kinematics has benefited from developments in DEM. For example, Oda and Iwashita (2000) developed a modified 2D DEM approach and laboratory biaxial experiments to investigate the onset of shear bands in granular materials. Oda and Iwashita (2000) defined plural bands as zones of intensive shear strains that develop during the hardening regime before the peak principal stress ratio (PSR). After the peak PSR, strain localization continues in one of these bands and a major persistent shear band develops. Column-like structures parallel to the major principal stress direction nucleated and collapsed during strain hardening and reemerged during strain softening by means of particle rotation. In addition, stress states were found to be different across shear band boundaries. Jiang et al. (2010) used the 2D distinct-element method to study strain localization of idealized sand in biaxial compression tests. They calculated velocity fields of individual particles based on changes in the particles' centroids and noticed inhomogeneous distribution of velocity fields during the hardening phase of simulations and the birth of several mini shear bands near the peak stress state that eventually evolved into a single major shear band after the phase-change point during DEM simulations. Kuhn (1999) used DEM modelling to investigate local void-based fabric parameters and identified thin obliquely trending bands as the predominant deformation structures, in which slip deformation was most intense. These thin structures, named micro bands, appeared at the beginning of the test and spontaneously throughout loading. Kuhn (1999) pointed out that, unlike shear bands, micro bands are relatively thin, with a thickness between $1.5d_{50}$ and $4d_{50}$, where d_{50} is the mean particle size, and are neither static nor persistent. Kuhn (2003) expanded on the DEM micro-band concept using strain gradients in granular materials and concluded that strain localization is not an isolated phenomenon and that micro bands (some of these bands are not persistent) develop before the final stationary band. These micro bands can be modeled using second-gradient linear models, whereas a more complex nonlinear model can predict the deformation profile of a nonpersistent shear band during the hardening regime.

Few researchers have found experimental evidence of micro shear bands (MSBs) within biaxial experiments using DIC. Based on surface observations in biaxial experiments, Rechenmacher (2006)

[1]Graduate Student, Dept. of Civil and Environmental Engineering, Univ. of Tennessee, 325 John Tickle Building, Knoxville, TN 37996. Email: samirrah@vols.utk.edu

[2]Engineer, VPD-Machine Performance Analysis, Caterpillar, Inc., 140009 Old Galena Rd., Peoria, IL 61552. Email: Druckrey_Andrew@cat.com

[3]Professor, Dept. of Civil and Environmental Engineering, Univ. of Tennessee, 325 John Tickle Building, Knoxville, TN 37996 (corresponding author). Email: Alshibli@utk.edu

[4]Associate Professor, Dept. of Civil and Architectural Engineering, Qatar Univ., Doha, Qatar. Email: Riyadh@qu.edu.qa

Note. This manuscript was submitted on August 23, 2017; approved on July 12, 2018; published online on November 16, 2018. Discussion period open until April 16, 2019; separate discussions must be submitted for individual papers. This paper is part of the ***Journal of Geotechnical and Geoenvironmental Engineering***, © ASCE, ISSN 1090-0241.

noticed that multiple and conjugate MSBs were initiated during the hardening regime, but the persistent final shear band was not fully obvious until the postpeak PSR softening phase of the experiment. Hall et al. (2010b) performed experiments on 2D discs using a Grenoble biaxial shear apparatus and captured multiple digital images of specimens' surface. DIC analyses revealed evidence of complex evolving internal structures consisting of bands of localized deformation and cells of low deformation between the bands. The bands developed during the early stage of shearing as the specimens approached the peak shear stress. A complex pattern of shear bands developed as shearing continued. Bouil et al. (2014) detected extremely small heterogeneous strains (on the order of 10^{-5}) using DIC in biaxial experiments, finding intermittent MSB development and subsequent collapse between 2.5% axial strain and the peak deviator stress at which a final persistent shear band dominates. In summary, different terminologies (plural bands, mini shear bands, micro bands, and MSBs) were used to describe the onset of structured localized deformations that develop sporadically during the hardening phase of a given experiment or DEM simulation and eventually lead to the development of a persistent shear band during the postpeak PSR and the critical state (CS).

Evidence of MSBs has been detected using DEM and DIC; however, conventional discrete particle kinematics calculate particle translation and/or rotation changes with reference to the initial unloaded state or the previous loading state to expose strain localization in sheared granular materials. They often fail to expose MSBs when local relative shear translation between particles is masked by larger displacements of particles using a global coordinate system as reference for calculations. Some researchers have attempted to improve the experimental methods using new concepts within the framework of continuum mechanics. Andò et al. (2012a, b) detected the onset and evolution of shear bands close to the peak PSR by displaying the direction of the movement of particles and differentiating the upward and downward movements. Desrues and Andò (2015) investigated the strain localization in granular materials using both continuum and particle-level scales to expose structures of localized strain within sand specimens that were subjected to moderately high confining pressures (100 and 300 kPa). They also studied the influence of particle aspect ratio and particle rotation to explain the difference in residual stress for sands with different shapes. The aspect ratio of a particle is defined as the ratio of the length of the major principal axis to the length of the minor principal axis.

Druckrey et al. (2018) studied the 3D kinematics of particles in triaxial experiments at different strain levels using SMT and particle tracking for F35 Ottawa sand. The second-order norm between a particle's translation field and its neighbors was averaged and used as a new relative particle translation gradient (RPTG) concept to uncover the onset of localized shearing. Alshibli et al. (2017) reported the results of SMT experiments on glass beads and three types of sand. Their analysis was limited to the use of particle translation and rotation to expose strain localization of sheared granular materials. As such, they were unable to detect MSBs during the hardening phase of the experiments, due to reasons described previously.

The methodology used in this paper adopts the RPTG concept developed by Druckrey et al. (2018) to analyze the SMT scans of the specimens reported by Alshibli et al. (2017). This paper focuses on investigating the effects of specimen density and confining pressure on the failure mode of specimens. The rotation of the particles is also studied as another particle kinematic measure affecting the deformation behavior of sheared granular materials. The evolution of the cumulative rotation angle (CRA) of particles is analyzed and discussed. In addition, the paper uses the average contact number (ACN) of individual sand particles as another indicator of the influence of particle morphology on particle-to-particle interaction.

Experiments

Four granular materials with different morphologies described by Alshibli et al. (2014) were used in this study. Grain-size distribution is not considered as a parameter in this study; therefore, only size fractions between 0.297 mm (US sieve #50) and 0.429 mm (US sieve #40) was used in the experiments. Three silica sands—F-35 Ottawa sand (F35), GS#40 Columbia grout sand (GS40), and #1 dry glass sand (DG)—and glass beads (GB) with a mean particle size (d_{50}) of 0.36 mm were used in the experiments. Sand systems used in this study represent uniform silica sands with different morphologies ranging from rounded to angular particle classes. Glass beads with similar grain size as these sands were also included in the investigation to provide baseline measurements for surface texture, roundness, and sphericity. Average microscale particle morphology properties of sphericity index (I_{sph}), roundness index (I_R), and surface texture (R_q) were introduced by Alshibli et al. (2014) and are summarized in Table 1. Sphericity (I_{sph}) and roundness (I_R) indexes of sand particles were based on 3D synchrotron microcomputed tomography images of particles. They are defined as

$$I_{\text{sph}} = \frac{V_p}{V_s} \tag{1}$$

$$I_R = \frac{A_p}{4\pi\left(\frac{d_L+d_I+d_s}{6}\right)^2} \tag{2}$$

where the denominator in Eq. (2) represents the surface area of a sphere that has a diameter equal to the average of the shortest (d_S), intermediate (d_I), and longest (d_L) lengths of the particles that pass through the center of mass of the particle; V_p and V_s = actual volume of the particle and volume of a sphere with a diameter equal

Table 1. Summary of experiments

Material	Experiment	Mean I_{sph}	Mean I_R	Mean R_q (μm)	Initial void ratio	σ_3 (kPa)	D_r (%)	Resolution (μm/voxel)
F-35 Ottawa sand	F35-L-15 kPa	1.872	0.959	2.084	0.668	15	49	8.16
	F35-D-15 kPa				0.603		83	11.14
	F35-D-400 kPa				0.586	400	91	11.18
#1 Dry glass sand	DG-L-15 kPa	1.704	0.937	1.990	0.799	15	64	8.16
	DG-D-15 kPa				0.754		83	11.14
	DG-D-400 kPa				0.727	400	95	11.18
GS#40 Columbia	GS40-D-15 kPa	1.674	0.924	1.923	0.721	15	89	11.14
grout sand	GS40-D-400 kPa				0.720	400	89	8.16
Glass beads	GB-D-15 kPa	1.096	0.965	0.381	0.690	15	96	11.14
	GB-D-400 kPa				0.687	400	99	11.18

J. Geotech. Geoenviron. Eng., 2019, 145(2): 04018104

to d_S, respectively; $I_{sph} = 1$ for a spherical particle; A_p = actual 3D surface area of the particle; and $I_R = 1$ for a particle that has no asperities/corners on its surface and has the same surface area as a sphere with an equivalent average diameter. Surface texture of sand particles was measured using optical interferometry technique according to the procedure described by Alshibli et al. (2014) and was calculated using the root mean square texture (R_q) as follows:

$$R_q = \sqrt{\frac{1}{MN}\sum_{i=1}^{M}\sum_{j=1}^{N} Z_{ij}^2} \tag{3}$$

where M and N = number of pixels in x- and y-directions; Z_{ij} = surface height at a specific pixel relative to the reference mean plane; and R_q = standard deviation of the surface heights.

The glass beads had an average I_{sph} of 1.096 and I_R of 0.965 (closest to unity for both I_{sph} and I_R, being the most spherical and least angular of the four granular materials) and had the smoothest surface texture, with a mean R_q of 0.381. F35 sand had the highest I_{sph} value (least spherical, $I_{sph} = 1.872$), followed by DG sand ($I_{sph} = 1.704$) and GS40 sand ($I_{sph} = 1.674$), which were relatively close in sphericity to each other. Of the three sands, F35 had a roundness index closest to unity ($I_R = 0.959$) after glass beads, followed by a more angular DG sand ($I_R = 0.937$) and the most angular GS40 sand ($I_R = 0.924$). F35 sand had the highest R_q value, followed by DG sand, GS40 sand, and glass beads.

A small triaxial apparatus described by Hasan and Alshibli (2012) and Druckrey and Alshibli (2014) was used in the experiments. A computer-controlled stepper motor was used to load the specimen at a constant displacement rate of 0.2 mm/min. Axial load was recorded using a load cell located inside the test cell. The load cell had a capacity of 400 N and an accuracy of 0.1 N. Air pressure was used to apply the desired confining pressure (σ_3). Axial deformation was measured from the stepper motor. The triaxial test cell was set up in Beamline 13BMD of the Advanced Photon Source (APS) at Argonne National Laboratory (ANL), Lemont, Illinois. Specimens were cylindrical and initially measured about 10 mm in diameter by 20 mm in height. Ten axisymmetric triaxial compression experiments were conducted on medium dense and very dense dry specimens under drained condition at two confining pressures, $\sigma_3 = 15$ and 400 kPa (Table 1). The prescribed σ_3 was applied to the specimens, and the apparatus was mounted on the stage of the X-ray beam for SMT imaging.

The advantages of SMT imaging were summarized by Druckrey et al. (2016), some of which are high resolution and sharp particle edges. Individual scans were acquired at multiple compression stages, pausing the experiment to collect 900 radiograph images at 0.2° rotation increments, which were reconstructed to create 3D SMT images. Resolutions of images are listed in Table 1. More information on image collection and reconstruction was given by Rivers (2012) and Rivers et al. (2010). An initial image was acquired, then the top end plate was moved at a constant compressive displacement rate of 0.2 mm/min to a predetermined target axial strain (ε_1), loading was paused, and the next image was acquired. It took approximately 50 min to collect one SMT scan. Particle kinematics can be determined between each of these incremental compressive displacements (or strains) as particles translate and rotate as a result of the global loading.

Image Processing and Particle Kinematic Analysis

SMT images showed that there was no particle fracture due to relatively low confining pressure values used in the experiments. The process of particle separation, tracking, and the necessary image enhancement steps were described in detail by Druckrey et al. (2016). Avizo Fire software (version 9.4) was initially used to process images by removing the noise, segmenting the images, and labeling particles. The physical location of each particle's voxels were stored in an $n \times 3$ matrix, where n is the number of voxels belonging to a particular particle. The three columns of the particle matrix were the x-, y-, and z-coordinates of the voxels that constitute the particle and can be easily used to calculate particle physical properties. Then, Druckrey's et al. (2016) code was used to measure the translation, rotation, and contact of particles within each SMT image. The translation of each particle was measured as the 3D vector that connected the centroid of each particle from multiple SMT images that were acquired at multiple ε_1 increments. The rotation of the particle was measured by calculating the angle between the particle's major axis and the direction of major principal stress (vertical direction). Absolute values of rotation angle were used in this study as an indicator of contact elimination or initiation of a new contact between particles.

Each particle label consists of connected voxels that have the same value, and each voxel occupied a cubical point in 3D space within the image. Identification of contact between particles involved analysis of the voxels belong to the surface of each particle. A matrix was generated that initially contained all voxels surrounding the particle surface. The voxels of the shell that did not contain another particle (the void space) were then removed from the matrix based on the labeled image. What remained in the matrix was the portion of the shell occupied by other particles in contact with the particle being analyzed. Furthermore, data can be extracted on each particle which was in contact with the particle being analyzed by searching the original labeled image for the particle identification number whose voxels occupied that space on the boundary. Coordination number was calculated as the total number of unique particle identification numbers within that matrix, which was the total number of particles in contact with the particle being analyzed. The CRA of each particle was calculated by taking the initial unloaded state as a reference for calculations.

Druckrey et al. (2018) introduced the concept of RPTG, which relates a particle translation vector ($\boldsymbol{\delta}$) to that of all neighboring particles in contact with that particle ($\delta_1, \delta_2, \ldots, \delta_n$), using the second-order norm of vector differences

$$rd_i = \text{norm}(\delta - \delta_i) \tag{4}$$

$$rd = \frac{1}{n}\sum_{i=1}^{n} rd_i \tag{5}$$

where rd_i = magnitude of relative translation for a single contacting neighboring particle; and n = number of contacting particles. The overall magnitude of relative translation is the average of all individual relative translation vectors (rd). The labeled images were used to track the changes of contact number (CN) for each particle. Rotation of particles was studied as one of the main causes of change in contact numbers. The CRA of each particle was measured as an indicator of the amount of rotation each particle underwent during the test. The absolute value of each increment's rotation angle was used in quantifying the CRA and thus a sign convention was not necessary.

Results

Axial compression and axial compressive loads were measured during the experiments, and the graphs of PSR versus ε_1 and

volumetric strain (ε_v) versus ε_1 were processed. Volume change of specimens was calculated from 3D SMT images. The size of specimens used in this study was relatively small. However, specimens contained enough particles to be representative of the material's behavior. Fig. 1 compares the GS40-D-400 kPa experiment and a similar GS40 specimen with an initial diameter of 71.1 mm and an initial height of 142.2 mm, showing an almost perfect match in ε_1 versus PSR relationship. The small difference in $\varepsilon_1 - \varepsilon_v$ relationship is attributed to different volume change measurements. The volume change of GS40-D-400 kPa was calculated from SMT images, whereas the volume change of the large triaxial specimen was measured from the volume of pore fluid displaced. In addition, there was a small difference in the specimens' densities.

Using sand with a narrow grain-size gradation caused the specimen to stay active as shearing continued, which explains a small volume increase as shearing continued. Batiste et al. (2004) and Alshibli et al. (2017) reported detailed investigations of failure modes of triaxial specimens that were monitored using the computed tomography imaging technique, which revealed that specimens continued to shear along secondary active shear bands as shearing continued. This paper provides a thorough analysis of the development and evolution of shear bands within specimens with different morphologies, density, and confining pressure.

At a relatively high confining pressure ($\sigma_3 = 400$ kPa), all specimens exhibited a gradual increase in PSR to a peak state, followed by a small softening. The DG sand specimen (DG-D-400 kPa) exhibited the highest peak PSR, 4.2, at $\varepsilon_1 = 7.1\%$, followed by a small amount of softening [Fig. 2(a)]. The F35-D-400 kPa sand specimen reached a peak PSR of 3.9 at $\varepsilon_1 = 5.1\%$, followed by relatively more softening. The GS40-D-400 kPa specimen closely followed F35-D-400 kPa, reaching a peak PSR of 3.8 at $\varepsilon_1 = 5.0\%$, followed by a small amount of softening. The glass bead specimen (GB-D-400 kPa) reached a peak PSR of 2.8 at $\varepsilon_1 = 3.7\%$, followed by a very small amount of softening. Of the four materials tested at $\sigma_3 = 400$ kPa, the DG-D-400 kPa experiment was the only specimen that did not exhibit a well-defined single shear band at the CS. Specimens tested at low confining pressure ($\sigma_3 = 15$ kPa) did not exhibit a peak PSR but rather an initial increase in PSR followed by a smaller rate of increase as compression progressed, leveling off at the CS (Figs. 3 and 4). The 400-kPa experiments exhibited a volume increase after a small initial contraction (Fig. 2), whereas the 15-kPa experiments dilated throughout the experiments, with no initial contraction (Figs. 3 and 4).

Incremental relative translation values of individual particles were calculated from the SMT images, for which the previous SMT image was taken as the reference for relative translation of particles in the current SMT image. Relative translations were normalized with respect to the incremental global axial displacement imposed by the top end plate for that strain increment. RPTG was calculated for all specimens, and the effects of confining pressure and density on the kinematics of the particle (cumulative rotation angle and translation gradient) are discussed in detail in the following subsections.

Failure Mode of Very Dense Specimens Tested at High Confining Pressure ($\sigma_3 = 400$ kPa)

Druckrey et al. (2018) reported the results of RPTG analysis for a very dense F35 Ottawa sand specimen tested at $\sigma_3 = 400$ kPa (F35-D-400 kPa specimen). Strain hardening took place between $\varepsilon_1 = 0\%$ and $\varepsilon_1 = 5.1\%$, and the specimen reached a peak PSR

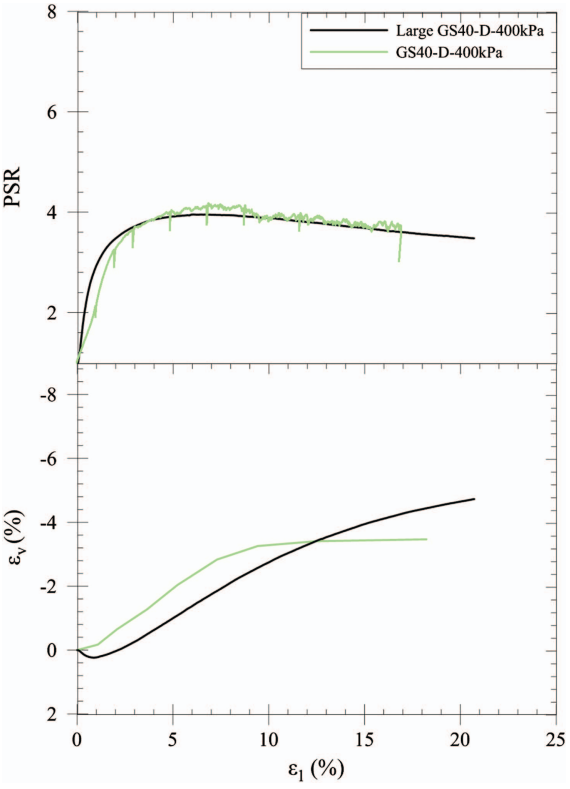

Fig. 1. (Color) Comparison between the behavior of GS40-D-400 kPa specimen ($D_r = 89\%$) and a similar specimen with initial diameter of 71.1 mm, initial height of 142.2 mm, and $D_r = 73\%$.

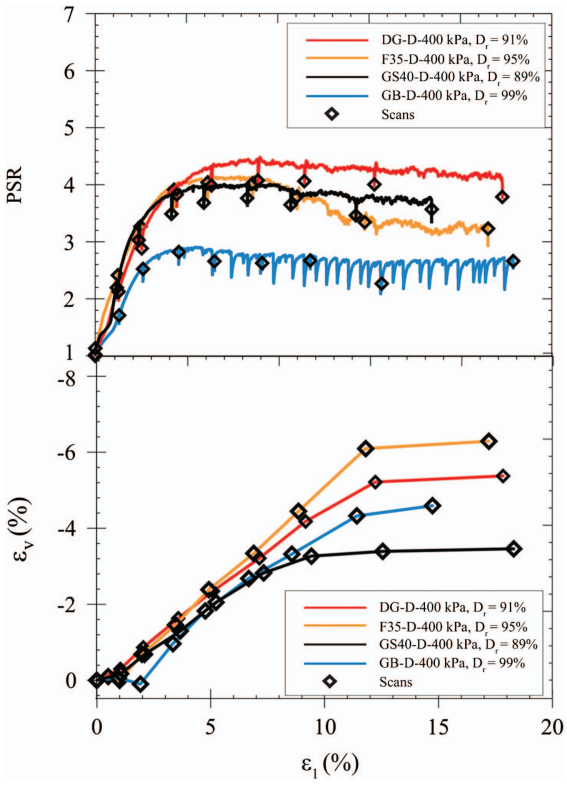

Fig. 2. (Color) Nominal axial strain versus principal stress ratio and volumetric strain for very dense specimens tested at high confining pressure ($\sigma_3 = 400$ kPa). (Reprinted from Alshibli et al. 2017, © ASCE.)

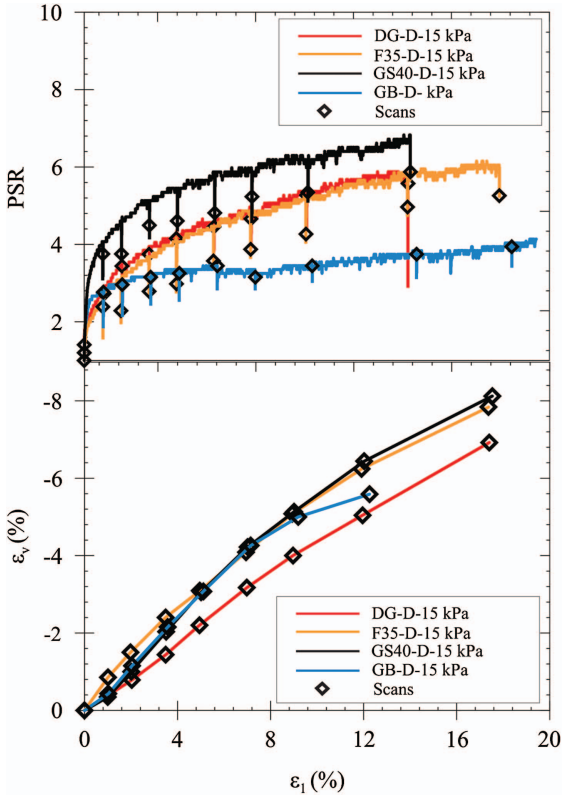

Fig. 3. (Color) Nominal axial strain versus principal stress ratio and volumetric strain for very dense specimens tested at low confining pressure ($\sigma_3 = 15$ kPa). (Reprinted from Alshibli et al. 2017, © ASCE.)

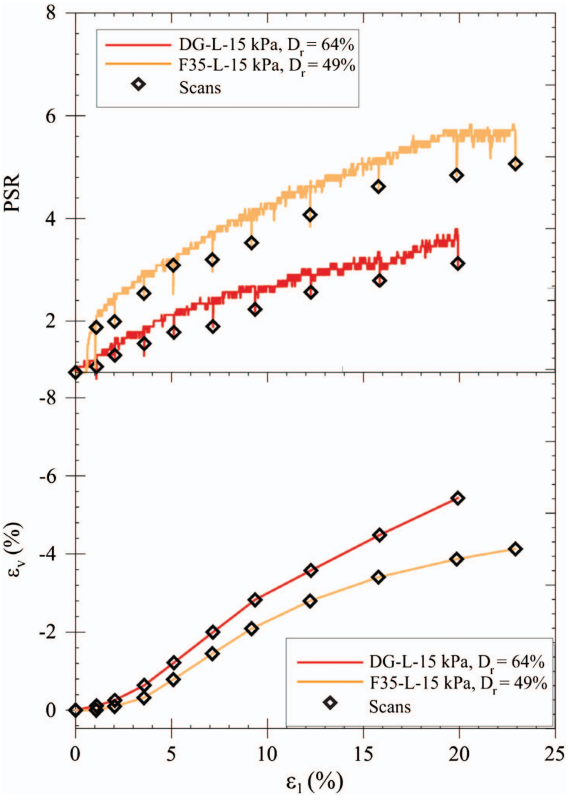

Fig. 4. (Color) Nominal axial strain versus principal stress ratio and volumetric strain for medium-dense specimens tested at low confining pressure ($\sigma_3 = 15$ kPa). (Reprinted from Alshibli et al. 2017, © ASCE.)

of 3.9 at $\varepsilon_1 = 5.1\%$ (Fig. 2). MSBs were detected during the hardening phase at $\varepsilon_1 = 0\%$–1% [Fig. 5(a)]. As the test progressed, MSBs continued to develop parallel and perpendicular to the direction of the final shear band. MSBs are shown in Fig. 5(b) after thresholding the color maps with values representing the average translation gradient of all particles within the cross section in Fig. 5(a) (i.e., deleting particles that exhibited relative translation gradients smaller than the average translation gradient of all particles within that slice). More MSBs developed at $\varepsilon_1 = 1.0\%$–2.0% [Fig. 5(c)]; they are shown in Fig. 5(d) through thresholding of color maps. It is evident that these MSBs increased in number, thickness, and length compared with the first loading step [Fig. 5(b)]. The MSBs became more defined, extending through the entire cross section of the specimen as compression progressed, and multiple MSBs merged to form a zone of intensive shearing at the center of the specimen at the end of the hardening phase [$\varepsilon_1 = 3.4\%$–4.9% Fig. 5(f)]. The orientation of the intensive shearing zone was the same as that of the final major shear band. Most MSBs merged to form the final major shear band as the specimen passed the peak PSR state [$\varepsilon_1 = 4.9\%$–6.9%, Fig. 5(g)]. The final major shear band became more defined during the postpeak PSR stage and had a thickness of $9d_{50}$–$10d_{50}$. Particles within this band exhibited high relative translations and were bound by transition bands composed of particles that manifested smaller relative translations.

The RPTGs for very dense glass beads that were tested at a high confining pressure (GB-D-400 kPa) are depicted in Fig. 6. Strain hardening took place in the range of $\varepsilon_1 = 0\%$–3.7%, peak PSR was reached between $\varepsilon_1 = 3.7\%$ and 4.0%, followed by softening in the range of $\varepsilon_1 = 4.0\%$–7.3%, and the CS transpired thereafter (Fig. 2). As in the F35-D-400 kPa experiment, zones of intensive shearing into MSBs were detected during the first ε_1 increment ($\varepsilon_1 = 0\%$–1%), and MSBs with thicknesses of $3d_{50} - 5d_{50}$ began to nucleate during the second ε_1 increment [$\varepsilon_1 = 1\%$–2.1%, Fig. 6(b)] and continued to grow throughout the hardening phase. MSBs are shown in Fig. 6(c) after the thresholding of the color map using average translation gradient of all particles within the cross section in Fig. 6(b). MSBs had a thickness of $3d_{50}$–$5d_{50}$. The thicknesses of MSBs in this experiment were larger than those observed in the F35-D-400 kPa experiment, and were not as well defined as those in the F35-D-400 kPa experiment. Most MSBs within the GB-D-400 kPa experiment oriented in the same direction as the final major shear band, whereas a few MSBs developed at the same inclination and the opposite direction as the final major shear band. During the peak PSR phase ($\varepsilon_1 = 3.7\%$–5.2%), most MSBs within the GB-D-400 kPa specimen merged into a large zone of intensive shearing within the specimen and oriented in the direction of the final major shear band. During the postpeak softening stage of the experiment ($\varepsilon_1 > 5.2\%$), the zone of intensive shearing localized into the final major single shear band that continued to evolve and develop during the CS. The final major shear band was much thicker (thickness = $13d_{50}$–$14d_{50}$) than that of the F35 sand that had a higher I_{sph} (least spherical), and more-angular and less-well-defined particles than the F35-D-400 kPa specimen. There were also some particles with large relative translation outside the final major shear band. Large relative translation of individual (or small groups of) particles outside MSBs or the final major shear bands was attributed to the stick-slip nature of glass beads, as manifested by frequent decreases in the PSR response in Fig. 2. Glass beads have relatively uniform roundness/sphericity and a smoother surface texture, which in turn reduces the interlocking and friction between particles. Once the PSR reaches the peak state; it forces the collapse of unstable force chains within the specimen, in which some of the particles within the force chains slide out of the chain due to low interlocking. The sliding manifests itself as oscillations

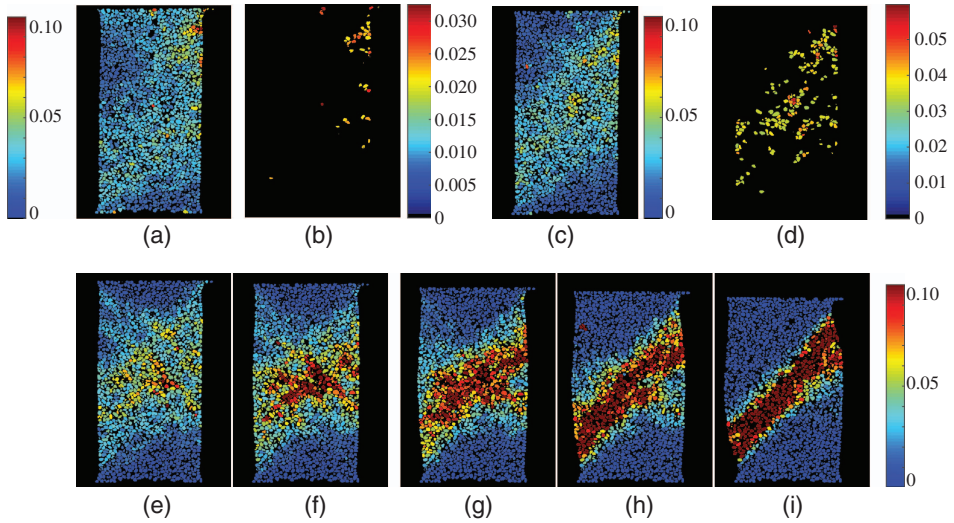

Fig. 5. (Color) Normalized relative particle translation gradient for F35-D-400 kPa: (a) $\varepsilon_1 = 0.0\%–1.0\%$; (b) $\varepsilon_1 = 0.0\%–1.0\%$, with particles that exhibited translation gradients smaller than the average translation gradient of all particles deleted to make MSBs more visible; (c) $\varepsilon_1 = 1.0\%–2.0\%$; (d) $\varepsilon_1 = 1.0\%–2.0\%$, with particles that exhibited translation gradients smaller than the average translation gradient of all particles deleted to make MSBs more visible; (e) $\varepsilon_1 = 2.0\%–3.4\%$; (f) $\varepsilon_1 = 3.4\%–4.9\%$; (g) $\varepsilon_1 = 4.9\%–6.9\%$; (h) $\varepsilon_1 = 6.9\%–8.9\%$; and (i) $\varepsilon_1 = 8.9\%–11.8\%$. Peak PSR is at $\varepsilon_1 = 5.1\%$; color bar represents value of normalized RPTG in decimal.

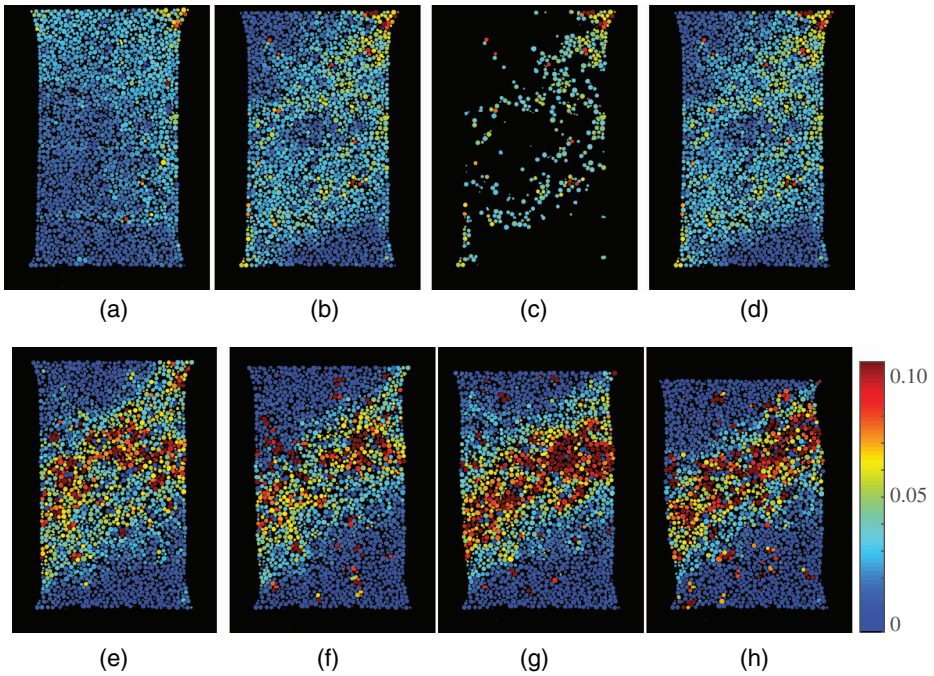

Fig. 6. (Color) Normalized relative particle translation gradient (RPTG) for GB-D-400 kPa: (a) $\varepsilon_1 = 0.0\%–0.1\%$; (b) $\varepsilon_1 = 1.0\%–2.1\%$; (c) $\varepsilon_1 = 1.0\%–2.1\%$, with particles that exhibited translation gradients smaller than the average translation gradient of all particles deleted to make MSBs more visible; (d) $\varepsilon_1 = 2.1\%–3.7\%$; (e) $\varepsilon_1 = 3.7\%–5.2\%$; (f) $\varepsilon_1 = 5.2\%–7.3\%$; (g) $\varepsilon_1 = 7.3\%–9.4\%$; and (h) $\varepsilon_1 = 9.4\%–12.5\%$. Peak PSR is at $\varepsilon_1 = 3.7\%$; color bar represents value of normalized RPTG in decimal.

in the PSR. Alshibli and Roussel (2006) presented a detailed experimental investigation of stick-slip phenomena in glass beads.

Fig. 7 displays the results of the RPTG for very dense GS#40 Columbia grout sand tested at high confining pressure (GS40-D-400 kPa). The experiment exhibited strain hardening until $\varepsilon_1 = 4.7\%$. Peak PSR phase for this experiment was broad and endured through Increments 5 and 6 ($\varepsilon_1 = 4.7\%–6.7\%$ and $6.7\%–8.6\%$, respectively), whereas slight softening occurred during Increment 7 ($\varepsilon_1 = 8.6\%–11.4\%$) and thereafter (Fig. 2). The initial ε_1 increment ($\varepsilon_1 = 0\%–1\%$) showed no evidence of MSBs; only two horizontal layers of larger relative displacement were apparent as a result of image processing and should not be considered as strain localization. Through Increments 2 and 3 ($\varepsilon_1 = 1.0\%–1.9\%$ and $1.9\%–3.3\%$, respectively) during the strain hardening phase, a complex

J. Geotech. Geoenviron. Eng., 2019, 145(2): 04018104

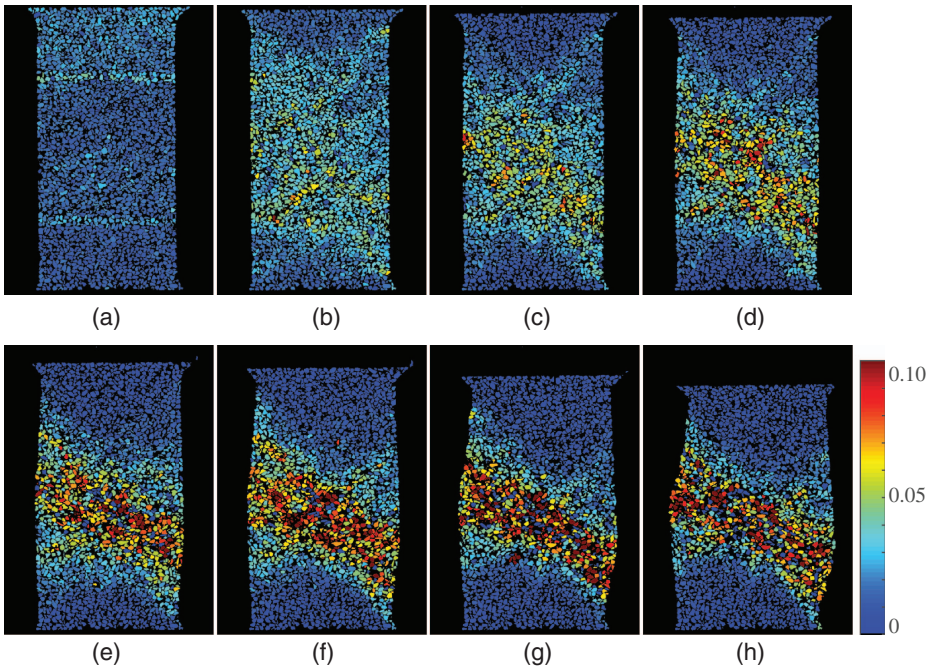

Fig. 7. (Color) Normalized relative particle translation gradient (RPTG) for GS40-D-400 kPa: (a) $\varepsilon_1 = 0.0\%$–1.0%; (b) $\varepsilon_1 = 1.0\%$–1.9%; (c) $\varepsilon_1 = 1.9\%$–3.3%; (d) $\varepsilon_1 = 3.3\%$–4.7%; (e) $\varepsilon_1 = 4.7\%$–6.7%; (f) $\varepsilon_1 = 6.7\%$–8.6%; (g) $\varepsilon_1 = 8.6\%$–11.4%; and (h) $\varepsilon_1 = 11.4\%$–14.7%; Peak PSR is at $\varepsilon_1 = 5.0\%$. Color bar represents value of normalized RPTG in decimal.

network of MSBs emerged similar to those in the F35-D-400 kPa experiment, with thicknesses of $2d_{50}$–$4d_{50}$. Many MSBs developed in conjugate directions with inclinations similar to that of the final major shear band, whereas some extended through the entire specimen. Near the end of strain hardening ($\varepsilon_1 = 3.3\%$–4.7%), the MSBs began to merge and show a preferential alignment with that of the final major shear band. During the peak PSR phase, few MSBs remained, and the final major shear band was nearly fully developed. Full development of the final major shear band commenced during the minor postpeak PSR softening and continued through the CS phase. The final major shear band for the GS40-D-400 kPa experiment had a thickness in the range of $10d_{50}$–$13d_{50}$ and was not as well-defined nor as delineated as the shear band for the F35-D-400 kPa experiment (thickness $9d_{50}$–$10d_{50}$). However, the final major shear band for the GS40-D-400 kPa experiment was more delineated and better defined than the shear band in the GB-D-400 kPa experiment (thickness $13d_{50}$–$14d_{50}$), indicating the influence of particle morphology on the growth of shear bands in granular materials.

The relatively high confining pressure is conducive to forcing shearing along a well-defined single shear band for a very dense specimen. Of the three 400 kPa experiments that exhibited a final major shear band, the thickness of the final shear band of F35 sand was the lowest, followed by that of GS40 sand; the final major shear band of glass beads was the thickest. This trend was also apparent for MSBs thicknesses, in which F35 sand had the thinnest MSBs, followed by GS40 sand and glass beads. A careful look at particle morphology values in Table 1 shows that F35 sand had the highest roughness (surface texture), highest nonsphericity, and second-highest roundness, excluding the GB. The GS40 sand particles were more spherical, more angular, and had a surface roughness lower than F35 sand. It appears that particle roundness and surface roughness are the main contributors to particle interlocking, relative particle translation, and specimen tendency to develop a shear band. Many glass beads will be part of the shear band, because they are spherical and have smooth surfaces; therefore, the rotation of particles during shearing is not suppressed due to friction and interlocking between particles. The high σ_3 and very dense packing will suppress the ability of nonspherical particles to rotate, and nonround corners (represented by I_R) contribute to a higher interlocking between particles, which will result in a slightly thicker shear band for GS40 sand than for F35 sand.

Pena et al. (2007) and Andò et al. (2012a, b) investigated the effect of particle shape on the rotation of particles and the thickness of the shear band. Pena et al. (2007) used a molecular dynamic approach to study the micromechanical behavior of 2D granular assemblies in a shear cell. A Voronoi tessellation scheme was used to create random 2D polygons (particles) within the periodic shear cell. The shear strain localization was investigated by quantifying the particle rotation along the height of the specimen. The distribution of average particle rotation along the height of the specimen was quantified. The thickness of the shear band was defined as the width of the distribution with a rotation angle higher than 80% of the maximum average rotation. They showed that the width of the localization zone in an isotropic medium is larger than the width of the localization zone in elongated particles (i.e., a ratio of 0.55–0.45 of the cell height).

According to Pena et al. (2007), the thinner shear bands in the elongated particles were attributed to the shape of the particles, which increased the interlocking and exhaustion of the movement of the particles, causing a thinner shear band. The 2D polygons used in their study had a smaller degree of freedom compared with particles within a 3D granular assembly. A smaller degree of freedom affects the relative translation between particles. The elongated particles in the medium had a uniform aspect ratio of 2.3, which is considered a high aspect ratio compared with the particles used in this paper. Another important element was the angularity of the isotropic and elongated particles used in Pena et al. (2007). Both isotropic and elongated particles had angular shapes, which increased the interlocking between the particles.

Andò et al. (2012b) used an ID-tracking method to investigate the 3D kinematic behavior of Hostun HN31 (angular grains, $d_{50} = 338$ μm) and Caicos ooids (rounded grains, $d_{50} = 420$ μm) sands in triaxial experiments. The tracking scheme is similar to the method used in this paper. The 3D translation and rotation particles were used to identify the shear bands within the specimens. They concluded that specimens with angular particles exhibited a thicker shear band than did specimens composed of rounded particles. They argued that this happens due to the interlocking between the particles, which expands the influence zone of the rotation of the particle. Because the influence zone is larger, the rotation of a particle affects a larger area and causes a thicker shearing zone. The findings of the present paper in terms of the influence of particle morphology agree in principle with Andò's et al. (2012a, b) explanation, keeping in mind that the present paper offers quantitative measurements of morphology indexes based on 3D images of sand grains.

RPTG for #1 dry glass sand tested at high confining pressure (DG-D-400 kPa experiment); results are displayed in Fig. 8. This experiment experienced strain hardening up to $\varepsilon_1 = 5\%$, peak PSR at $\varepsilon_1 = 6.9\%$, and a very minor softening into the CS during Increment 6 ($\varepsilon_1 = 6.9\%$–8.9%) (Fig. 2). Failure of this specimen was characterized as bulging based on the specimen's surface deformation, which is an external manifestation of a more complex internal failure mode. Strain localization began to form during the first ε_1 increment ($\varepsilon_1 = 0\%$–1%) (Fig. 8). In the second ε_1 increment ($\varepsilon_1 = 1\%$–2%), MSBs formed in a diagonal direction through the specimen, which would seem to be early evidence of a major well-defined single shear band. However, during the third ε_1 increment ($\varepsilon_1 = 2\%$–3.5%), several MSBs developed throughout the specimen in the opposite direction and began to compete with the previously developed MSBs. MSBs in this third increment had thicknesses of $3d_{50}$–$4d_{50}$. During the fourth ε_1 increment ($\varepsilon_1 = 3.5\%$–5%), a complex network of MSBs emerged with a preferential inclination; however, intersecting MSB caused a relatively large zone of intensive shearing within the middle of the specimen. During the loading increment approaching peak PSR ($\varepsilon_1 = 5\%$–6.9%), MSBs developed in opposite directions, resulting in the development of two conical shearing surfaces near the specimen's top and bottom and an intensive shearing zone in its middle. Conflicting MSBs in a cross-hatched pattern continued to compete with each other throughout the remainder of the experiment, retaining the conical shearing zones near the top and bottom of the specimen and many MSBs in the central zone. Cross-hatching of MSBs forced other lateral MSBs to manifest and push outward toward the specimen surface and to push groups of particles outward, resulting in specimen bulging at the surface. During the last two ε_1 increments ($\varepsilon_1 = 8.9\%$–17.4%, Fig. 8), particles within the sheared central part of the specimen experienced large translations which made it difficult to track most particles within that zone, so the translation gradient is not displayed for these particles.

DG sand had the highest angularity of surface corners according the o roundness classification (Table 1), which appears to be the main morphology index affecting strain localization of very dense specimens tested under high confining pressure. In addition, it had the second-highest I_{sph} and R_q values. As the specimen tried to fail along a single shear band, a high degree of interlocking developed, causing a high resistance to shearing that forced the development of multiple NSBs and a zone of high dilation in the middle part of the specimen. Compared with the other specimens in Fig. 2, DG-D-400 kPa exhibited the smallest softening because it continued to resist shearing with a high degree of interlocking between particles, whereas a single shear band caused a decrease in PSR for F35-D-400 kPa.

Failure Mode of Very Dense Specimens Tested at Low Confining Pressure ($\sigma_3 = 15$ kPa)

The failure mode of very dense specimens sheared at a low confining pressure ($\sigma_3 = 15$ kPa) occurred through bulging, based on observations of specimen surface. The F35-D-15 kPa experiment

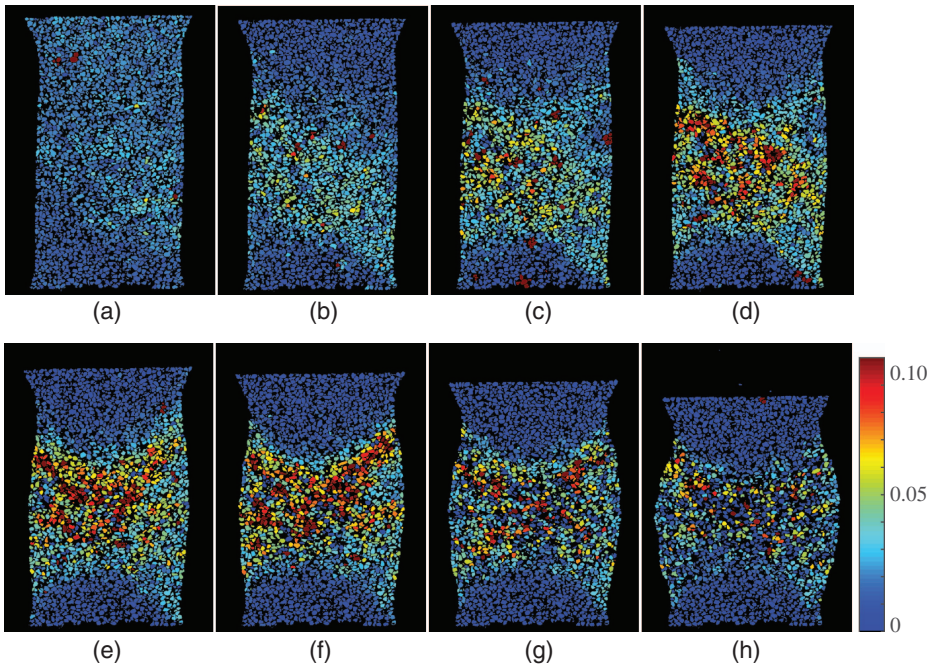

Fig. 8. (Color) Normalized relative particle translation gradient (RPTG) for DG-D-400 kPa: (a) $\varepsilon_1 = 0.0\%$–1.0%; (b) $\varepsilon_1 = 1.0\%$–2.0%; (c) $\varepsilon_1 = 2.0\%$–3.5%; (d) $\varepsilon_1 = 3.5\%$–5.0%; (e) $\varepsilon_1 = 5.0\%$–6.9%; (f) $\varepsilon_1 = 6.9\%$–8.9%; (g) $\varepsilon_1 = 8.9\%$–11.9%; and (h) $\varepsilon_1 = 11.9\%$–17.4%; Peak PSR is at $\varepsilon_1 = 7.1\%$; color bar represents value of normalized RPTG in decimal.

J. Geotech. Geoenviron. Eng., 2019, 145(2): 04018104

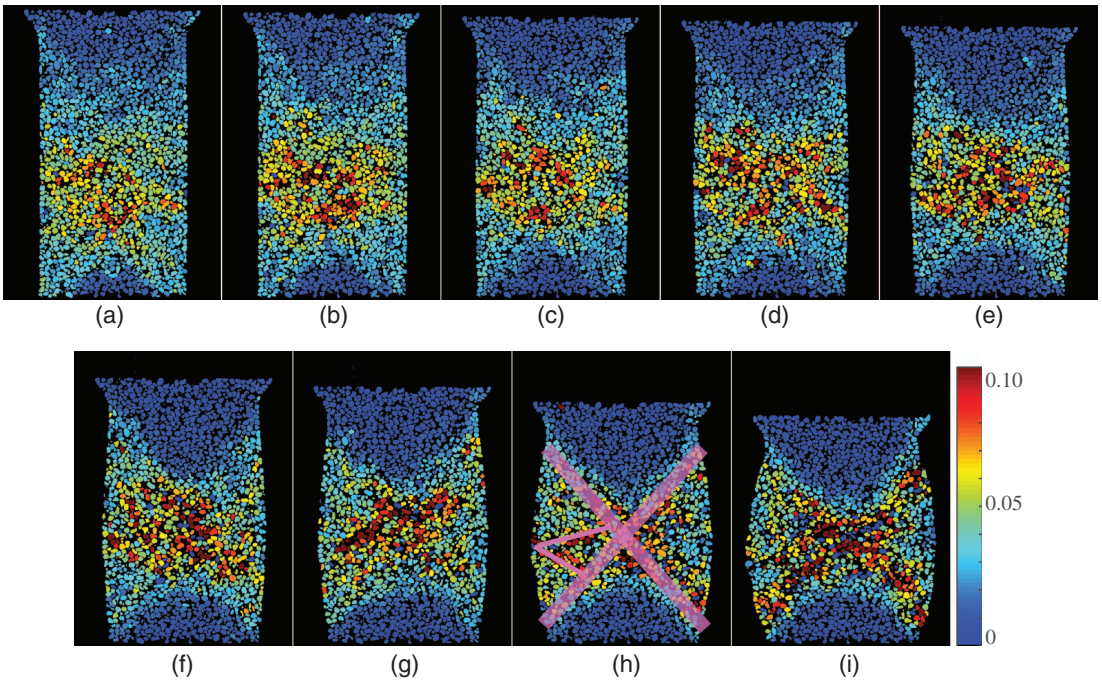

Fig. 9. (Color) Normalized relative particle translation gradient (RPTG) for F35-D-15 kPa: (a) $\varepsilon_1 = 0.0\%$–1.0%; (b) $\varepsilon_1 = 1.0\%$–2.0%; (c) $\varepsilon_1 = 2.0\%$–3.5%; (d) $\varepsilon_1 = 3.5\%$–5.0%; (e) $\varepsilon_1 = 5.0\%$–6.9%; (f) $\varepsilon_1 = 6.9\%$–8.9%; (g) $\varepsilon_1 = 8.9\%$–11.9%; (h) $\varepsilon_1 = 11.9\%$–17.4%; and (i) $\varepsilon_1 = 17.4\%$–22.3%. Color bar represents value of normalized RPTG in decimal.

(Fig. 9) showed early signs of randomly oriented MSBs with thicknesses in a range between $2d_{50}$ and $3.5d_{50}$ concentrated in the central part of the specimen until approximately $\varepsilon_1 = 3.5\%$–5%, when MSBs had mostly merged into a centralized zone except for the conical shearing zones near the top and bottom of the specimen. As shearing progressed, a centralized hourglass-like (X-shaped in 2D slice visualizations) shearing pattern dominated the internal microstructure, forcing particles to move toward the surface of the specimen in the lateral direction, and some of these particles were part of MSBs (Fig. 9, $\varepsilon_1 = 11.9\%$–17.4%); thick transparent markers were added to the image to show the hourglass pattern, and the thin lines show structured MSBs being forced outward. The outward thrust of particles and MSBs caused surface bulging of the specimens. Fig. 10 displays cross-sectional slices within the conical shearing zones at the top and bottom of the specimen as well as a cross section near the midheight of the specimen for the $\varepsilon_1 = 11.9\%$–17.4% increment. The circular pattern within the top and bottom cross-sectional slices revealed that the shape of the failure zone was in fact conical. The middle axial cross-section slice shows the high RPTG between the conical shearing zones and multiple MSBs with no preferred orientation other than random RPTGs toward the circumference of the specimen in the lateral direction (specimen's axisymmetric plane).

The GS40-D-15 kPa experiment (Fig. 11) also exhibited early signs of MSB development (thicknesses between $3.5d_{50}$ and $4d_{50}$) and retained several major MSBs after $\varepsilon_1 = 5\%$ with inclinations similar to the conical shape observed near the top and bottom of the F35-D-15 kPa experiment, resulting in a centralized cross-hatched shearing pattern. The ends of the MSBs pushed toward the specimen surface, and particles outside those shearing zones were forced to move outward laterally, resulting in bulging of the specimen surface. A similar failure mode was observed in the DG-D-15 kPa experiment at early strains (Fig. 12), with MSB thicknesses between $3d_{50}$ and $3.5d_{50}$. A cross-hatched MSB pattern formed, and conical

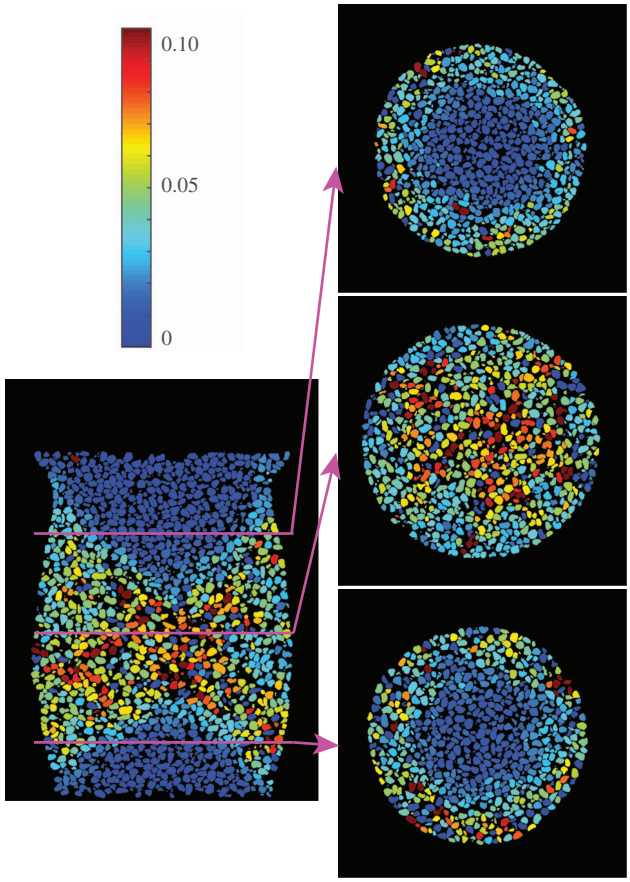

Fig. 10. (Color) Axial section of F35-D-15 kPa at strain increment $\varepsilon_1 = 11.9\%$–17.4%. Color bar represents the value of normalized RPTG in decimal.

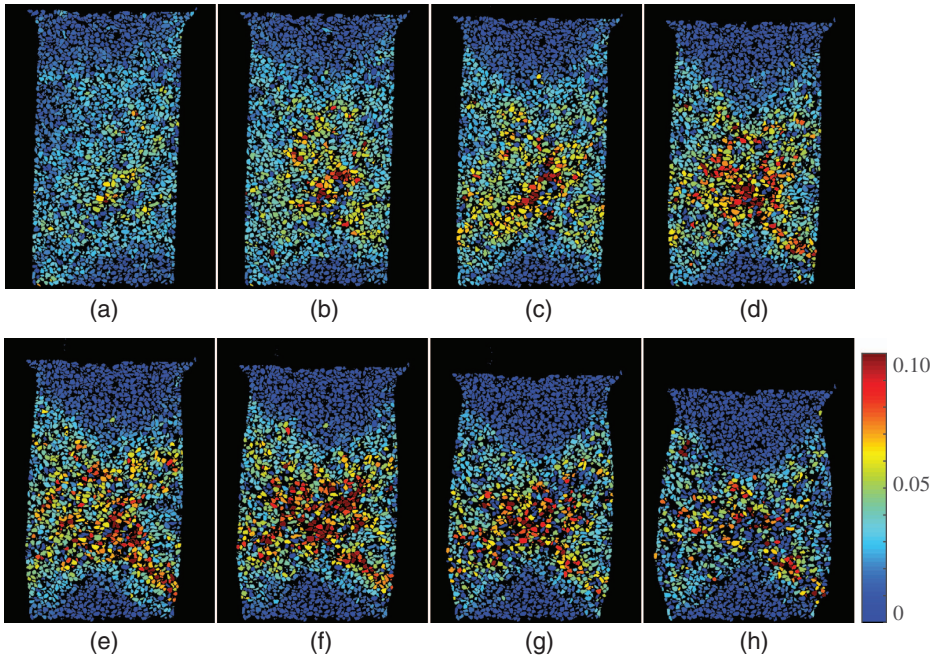

Fig. 11. (Color) Normalized relative particle translation gradient (RPTG) for GS-D-15 kPa: (a) $\varepsilon_1 = 0.0\%–1.0\%$; (b) $\varepsilon_1 = 1.0\%–2.0\%$; (c) $\varepsilon_1 = 2.0\%–3.5\%$; (d) $\varepsilon_1 = 3.5\%–5.0\%$; (e) $\varepsilon_1 = 5.0\%–7.0\%$; (f) $\varepsilon_1 = 7.0\%–9.0\%$; (g) $\varepsilon_1 = 9.0\%–12.0\%$; and (h) $\varepsilon_1 = 12.0\%–17.5\%$. Color bar represents value of normalized RPTG in decimal.

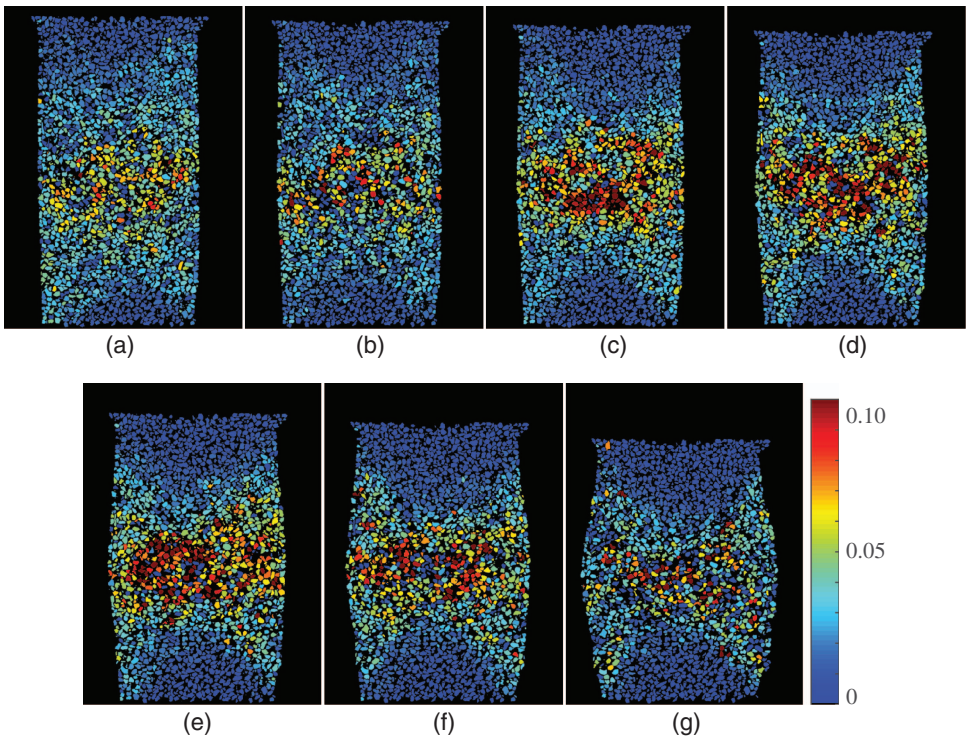

Fig. 12. (Color) Normalized relative particle translation gradient (RPTG) for DG-D-15 kPa: (a) $\varepsilon_1 = 0.0\%–2.0\%$; (b) $\varepsilon_1 = 2.0\%–3.5\%$; (c) $\varepsilon_1 = 3.5\%–5.0\%$; (d) $\varepsilon_1 = 5.0\%–6.9\%$; (e) $\varepsilon_1 = 5.0\%–6.9\%$; (f) $\varepsilon_1 = 6.9\%–11.9\%$; and (g) $\varepsilon_1 = 11.9\%–17.4\%$. Color bar represents value of normalized RPTG in decimal.

shearing zones at the top and bottom of the specimen developed and persisted. However, particle relative translation eventually showed a large centralized zone of particle intensive shearing pushing particle groups outward laterally to cause specimen bulging. The GB-D-15 kPa experiment (Fig. 13) exhibited many distributed MSBs and zones of localized shearing throughout the experiment, many of which were sporadically distributed throughout the specimen. Thicknesses of MSBs at early strain increments were between

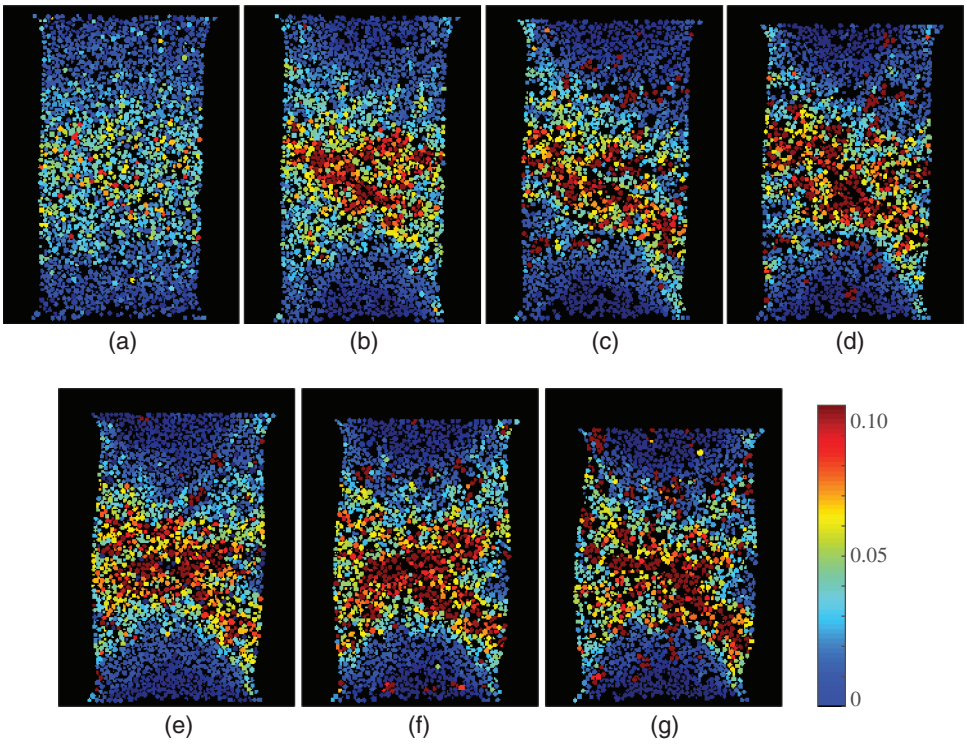

Fig. 13. (Color) Normalized relative particle translation gradient (RPTG) for GB-D-15 kPa: (a) $\varepsilon_1 = 0.0\%$–1.0%; (b) $\varepsilon_1 = 1.0\%$–2.0%; (c) $\varepsilon_1 = 2.0\%$–3.6%; (d) $\varepsilon_1 = 3.6\%$–5.1%; (e) $\varepsilon_1 = 5.1\%$–7.1%; (f) $\varepsilon_1 = 7.1\%$–9.2%; and (g) $\varepsilon_1 = 9.2\%$–12.2%. Color bar represents value of normalized RPTG in decimal.

$3d_{50}$ and $5d_{50}$. Some structure was retained in cross-hatched MSBs; however, some of the structured deformation was randomly orientated, and shearing zones near the specimen top and bottom did not have a well-defined conical structure. Specimen bulging was caused by MSB ends pushing out toward the specimen surface as well as pushing groups of particles laterally outward.

The role of confining pressure on internal shearing mechanisms of granular material was significant. A cross-hatched MSB failure pattern developed during strain hardening for both low ($\sigma_3 =$ 15 kPa) and high ($\sigma_3 = 400$ kPa) confining pressures. However, at low confining pressure, MSBs were thicker, and shearing zones were not as well structured as they were at higher confining pressure. This is attributed to a more stable microstructure imposed by higher confining pressure. A high confining pressure typically forced MSBs and shearing zones to merge into a single major shear band during the peak PSR and softening phases, except in the DG-D-400 kPa experiment. In experiments conducted at low confining pressure, the failure manifested in specimen surface bulging with a complex network of internal MSBs. Cross-hatched MSBs were the typical mode of the internal failure (singular hourglass pattern in the F35-D-15 kPa experiment), in which the cross-hatched MSBs forced groups of particles and lateral MSBs outward as well as conical shearing zones at the specimen top and bottom.

Failure Mode of Medium Dense Specimen Tested at Low Confining Pressure ($\sigma_3 = 15$ kPa)

Density plays a role similar to that of confining pressure on the mechanisms of shearing. Figs. 14 and 15 show the results for the F35-L-15 kPa and DG-L-15 kPa experiments in which evidence of the onset of MSBs was detected at early loading stages of the experiments ($\varepsilon_1 = 2\%$, Fig. 3). Sporadic MSBs were detected during early loading stages of both experiments with thicknesses between $3d_{50}$ to $5d_{50}$ (Figs. 14 and 15). As the experiments progressed, the MSBs evolved into less-defined geometric patterns compared with the patterns observed in dense specimens. This can be caused by the less-stable fabric in medium-dense specimens, in which there is relatively more void space between particles coupled with a low confining pressure. The failure mechanism in both specimens was manifested through a complex network of MSBs, which was very close to the failure mode of the F35-D-15 kPa and DG-D-15 kPa experimental results (X-shaped hourglass, Figs. 10 and 12). MSB orientations were random during the hardening phase of the experiments and transitioned into a more defined zone of intensive shearing composed of multiple MSBs.

Evolution of Particle Average Contact Number with Shear

In order to investigate the effect of particle kinematic behavior on particle-scale contact and interaction of particles within triaxial specimens, the evolution of average contact numbers of individual particles and their corresponding rotations were investigated. While rotating, particles may initiate new contacts and eliminate others. The dynamics of contacts (i.e., the number of contacts lost and created) is related to the degree of rotation, void space around particles, particle morphology, initial density of the specimen, and applied confining pressure. The effects of CRAs, specimen density, confining pressure, and particle aspect ratio on ACN were studied in detail using 3D measurements. The aspect ratio of particles was divided into three size categories, 1–1.75, 1.75–2.5, and greater than 2.5, based on the range of measurements of tested sands. Most particles had aspect ratios between 1 and 2.5. The CRA color map for particles within a central axial section perpendicular to the final shear bands is depicted in Fig. 16. The glass beads are excluded from Fig. 16 because of the lack of a meaningful trend within the specimens.

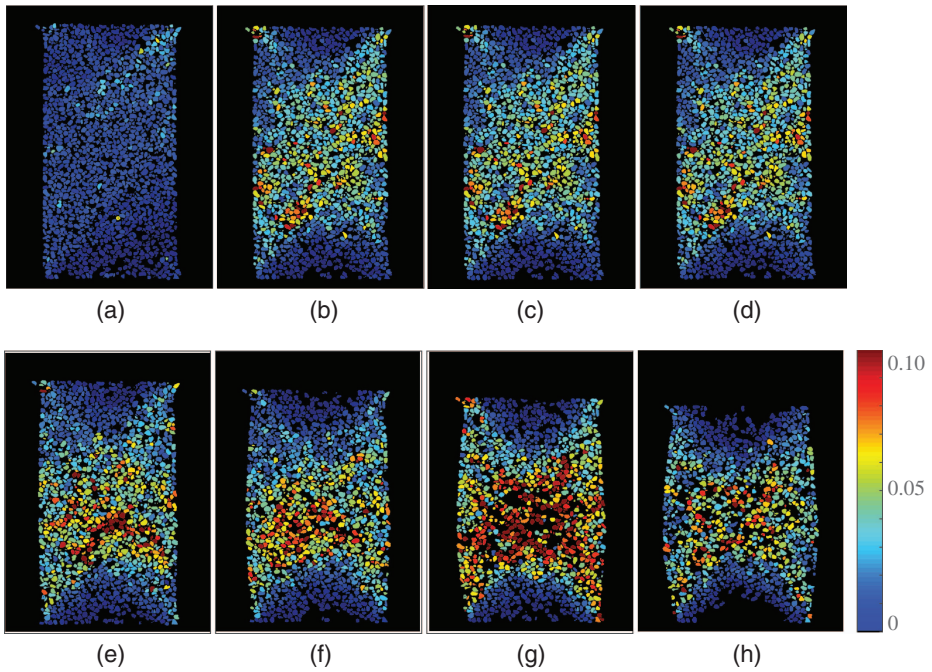

Fig. 14. (Color) Normalized relative particle translation gradient (RPTG) for F35-L-15 kPa: (a) $\varepsilon_1 = 0.0\%$–1.0%; (b) $\varepsilon_1 = 1.0\%$–2.0%; (c) $\varepsilon_1 = 2.0\%$–3.5%; (d) $\varepsilon_1 = 3.5\%$–5.1%; (e) $\varepsilon_1 = 5.1\%$–7.1%; (f) $\varepsilon_1 = 7.1\%$–9.5%; (g) $\varepsilon_1 = 9.5\%$–12.2%; and (h) $\varepsilon_1 = 12.2\%$–15.2%. Color bar represents value of normalized RPTG in decimal.

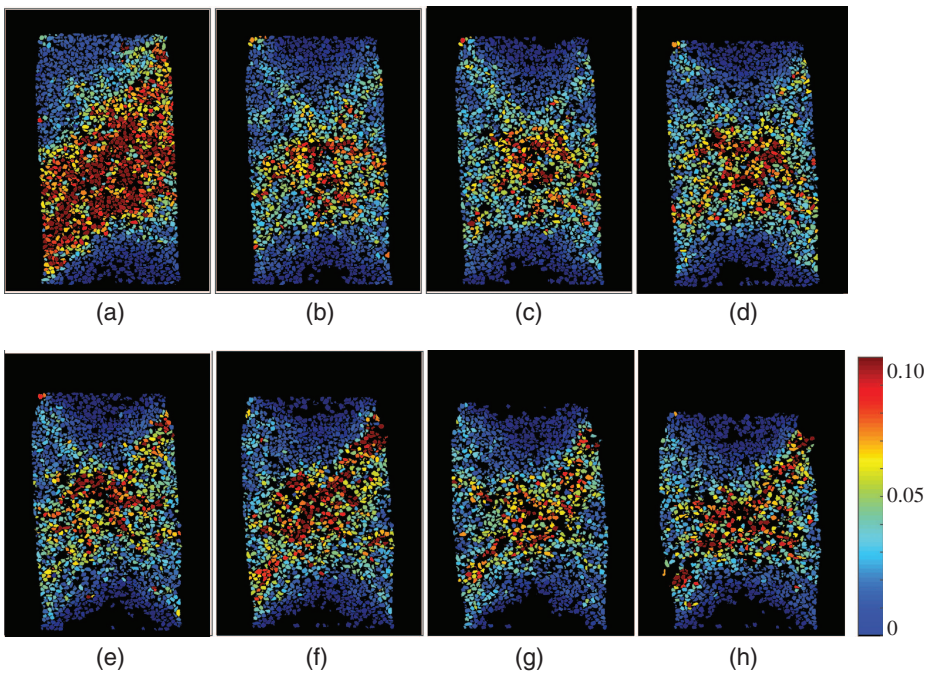

Fig. 15. (Color) Normalized relative particle translation gradient (RPTG) for DG-L-15 kPa: (a) $\varepsilon_1 = 0\%$–1.0%; (b) $\varepsilon_1 = 1.0\%$–2.0%; (c) $\varepsilon_1 = 2.0\%$–3.5%; (d) $\varepsilon_1 = 3.5\%$–5.1%; (e) $\varepsilon_1 = 5.1\%$–9.1%; (f) $\varepsilon_1 = 9.1\%$–12.2%; (g) $\varepsilon_1 = 12.2\%$–15.8%; and (h) $\varepsilon_1 = 15.8\%$–19.9%. Color bar represents value of normalized RPTG in decimal.

Particles within shear bands or within zones of intensive shearing exhibited higher rotation angles than particles outside these shear zones. Some particles rotated as much as 40°–50°. The number of particles that exhibited a high rotation increased as the confining pressure decreased for very dense specimens (Fig. 16, compare F35-D-15 kPa, DG-D-15 kPa, and GS40-D-15 kPa with F35-D-400 kPa, DG-D-400 kPa, and GS40-D-400 kPa, respectively).

In order to investigate the effect of CRA on the ACN of particles, the CRA was divided into three subgroups, and the evolution of the ACN of each subgroup was examined as the experiments

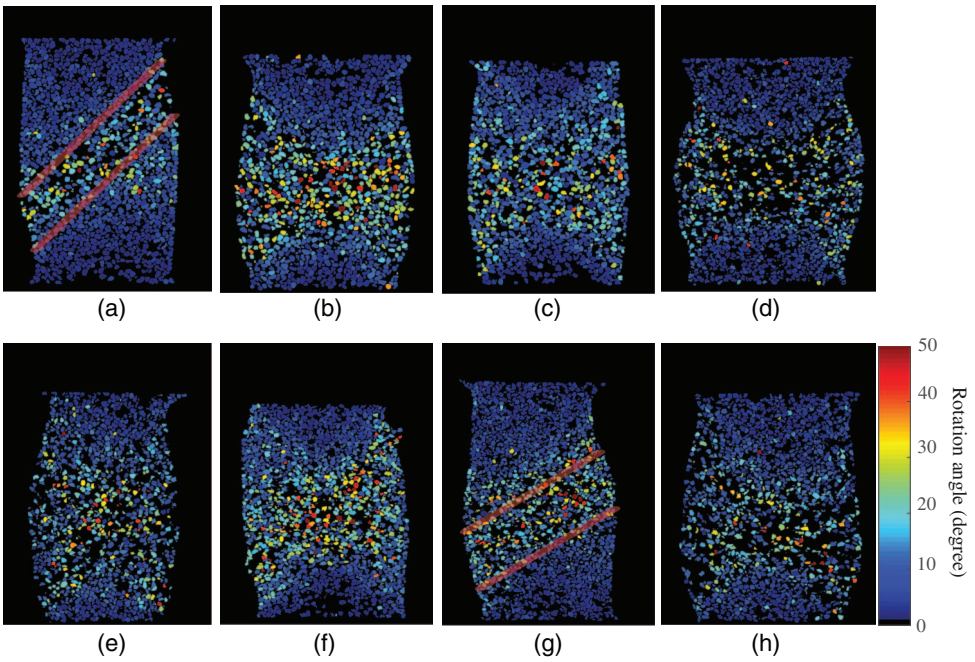

Fig. 16. (Color) Summary of cumulative rotation angle of tested sand specimens at end of experiments, with boundaries of major final shear bands highlighted by maroon lines: (a) F35-D-400 kPa; (b) F35-D-15 kPa; (c) F35-L-15 kPa; (d) DG-D-400 kPa; (e) DG-D-15 kPa; (f) DG-L-15 kPa; (g) GS40-D-400 kPa; and (h) GS40-D-15 kPa.

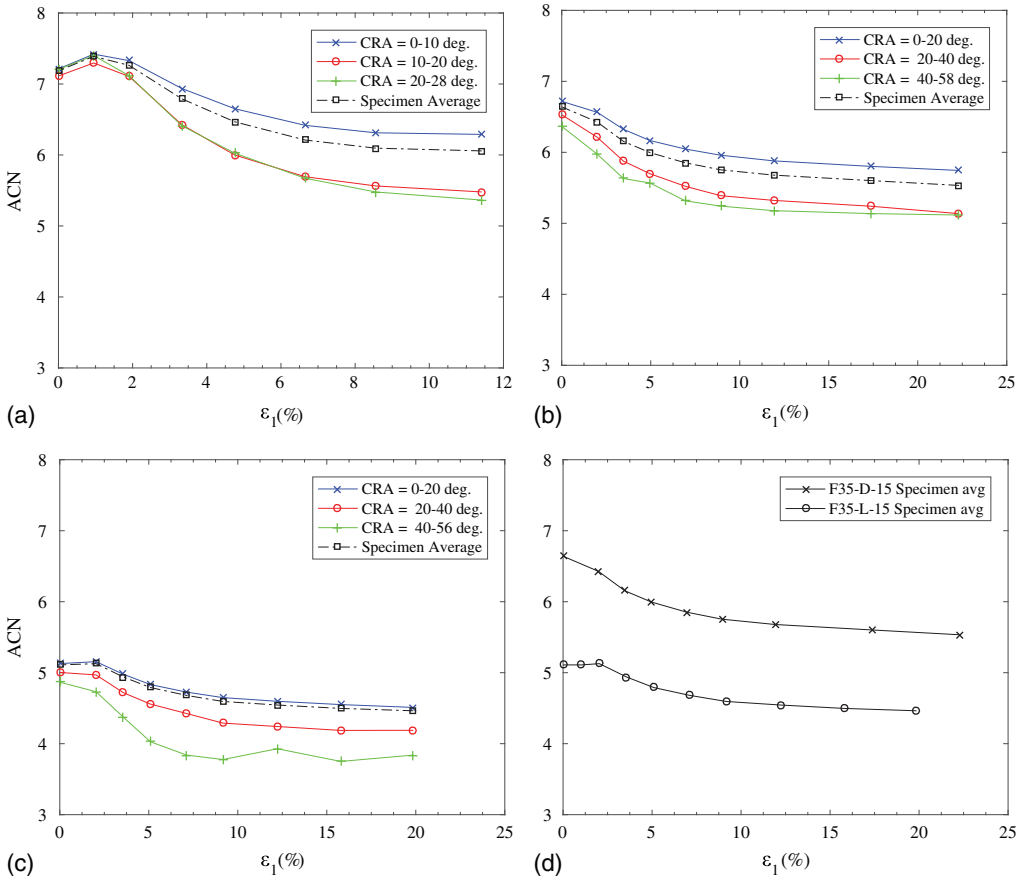

Fig. 17. (Color) Average contact number of F35 specimens: (a) F35-D-400 kPa experiment; (b) F35-D-15 kPa experiment; (c) F35-L-15 kPa experiment; and (d) F35-D-15 kPa versus F35-L-15 kPa.

progressed. F35 specimens (Fig. 17) had different ranges of CRA depending on initial specimen density and confining pressure. The F35-D-400 kPa specimen [Fig. 17(a)], which had a high initial density and was exposed to a high confining pressure ($\sigma_3 = 400$ kPa), exhibited smaller CRA, in the range between 0° and 28°, compared with F35-D-15 kPa [Fig. 17(b)], and F35-L-15 kPa [Fig. 17(c)], which had CRA values, ranging between 0° and 58° and 0° and 56°, respectively. The smaller void space and relatively high confining pressure for the F35-D-400 kPa specimen reduced particle rotation, manifesting rotations considerably smaller than those of the F35-L-15 kPa and F35-D-15 kPa specimens. For all three F35 specimens, particles with fewer contacts during the initial state (smaller ACN) had more freedom to rotate and exhibited higher CRA values. In addition, particles with higher CRA lost more contacts with their neighboring particles (highest change in the ACN) than did particles with smaller CRA as the shearing progressed. The high initial ACN during shearing supports the notion that smaller rotation angles are due to higher interaction with neighboring particles. Fig. 17(d) compares the evolution of ACN for F35 specimens with different initial densities. The ACN of particles in both the F35-L-15 kPa and F35-D-15 kPa specimens approached a plateau during the final stages of both experiments when the CS was reached. Rothenburg and Kruyt (2004) investigated the evolution of CN using DEM simulation of 2D granular discs and showed that the CN reached a constant value (i.e., critical contact number) during the final stages of the DEM simulations. The initial CN value for the dense specimens was higher than the CN for the medium-dense specimen, which was expected [Fig. 17(d)].

The variation of the ACN within the medium-dense specimen was much less than the change in the ACN of the very dense specimen. This difference was caused by extra void space around sand particles within the medium-dense specimen. The CN of particles is influenced by the void space available around them. Particles surrounded by more void space have a higher chance of forming new contacts compared with densely packed particles. The rate of contacts loss was much higher than the rate of forming new contacts in very dense specimens; thus the contact number varied noticeably. However, these two rates balanced each other in a medium-dense specimen, reducing the rate of change of ACN compared with that of a very dense specimen. Rothenburg and Kruyt (2004) investigated the effects of available void space around particles and formulated an analytical solution for the variation of CN that showed that the rate of formation of new contacts depends on the available void space around particles. In the present study, the F35-D-400 kPa specimen exhibited an initial increase in the can, followed by a significant decrease in the ACN as the test progressed. The F35-D-15 kPa specimen exhibited a gradual decrease in ACN throughout the test. Both dense specimens exhibited relatively similar ACNs in the initial stage and the final stage. Mirghasemi et al. (1997) studied the effects of confining pressure on the evolution of the CN of 2D polygon-shaped

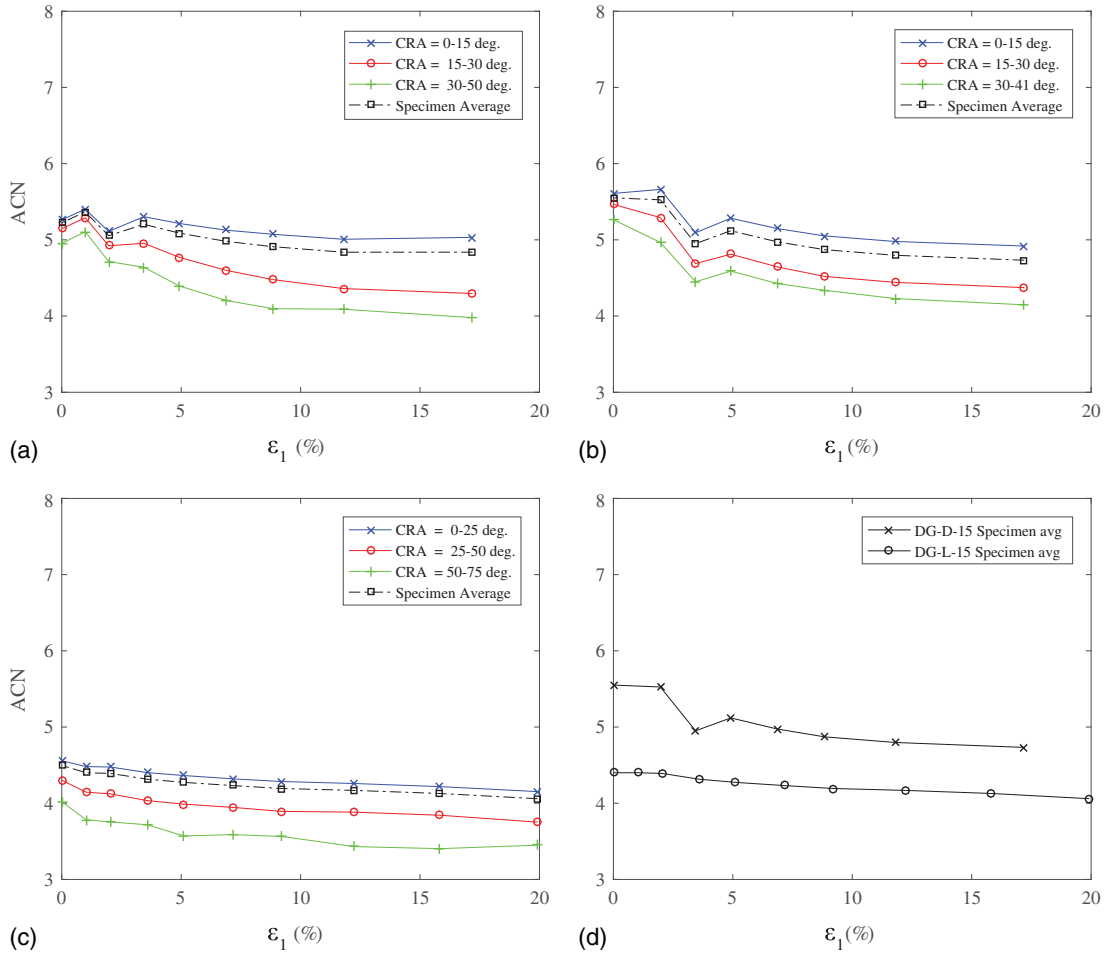

Fig. 18. (Color) Average contact number of DG specimens: (a) DG-D-400 kPa experiment; (b) DG-D-15 kPa experiment; (c) DG-L-15 kPa experiment; and (d) DG-D-15 kPa versus DG-L-15 kPa.

J. Geotech. Geoenviron. Eng., 2019, 145(2): 04018104

particles using DEM. They found that the confining pressure has similar effects as initial density of the specimens on the ACN of particles.

Fig. 18 shows the evolution of ACN of DG specimens, in which the range of CRA for the DG specimens and their dependence on the confining pressure and initial density was similar to that of the F35 specimens, except in the DG-D-400 kPa experiment, in which the range of rotation angle was slightly larger than that of the DG-D-15 kPa experiment even though σ_3 was much smaller for the DG-D-15 kPa experiment. The number of particles in DG-D-15 kPa with a CRA between 30° and 41° was very low (38 particles). Similar to the F35 specimens, particles with high CRA in the DG specimens had a smaller initial CN, and the CN continued to decrease as compression progressed, indicating the dependence of CRA on the initial specimen density and the evolution of ACN through the test. Figs. 18(a and b) show the ACN for the DG-D-400 kPa and DG-D-15 kPa experiments, respectively; σ_3 had little effect on the ACN of the DG specimens, which is similar to the results of F35 specimens. Fig. 18(c) summarizes the evolution ACN for the DG-L-15 kPa experiment, in which the rate of change of ACN was much smaller than the ACN for very dense specimens, supporting the dependence of the rate of change of ACN on the free void space available around particles. Fig. 18(d) compares the ACN for DG-D-15 kPa and DG-L-15 kPa specimens, showing that both specimens reached a critical ACN during the final stages of the experiments.

Fig. 19 shows the evolution of the ACN for the GS40 and GB specimens, only very dense specimens of which were scanned. The results are similar to those of the F35 and DG specimens, with the exception of the GB-D-400 kPa specimen, for which the rate of change of the ACN values was much less than that of other very dense specimens that were tested at high confining pressures. The GB specimens exhibited a higher CRA than the other specimen (as high as 300°). The GB particles were nearly spherical with no corners and had a relatively smoother surface, resulting in minimal interlocking between them. The absence of interlocking caused the particles to have more freedom to rotate compared with the other specimens. Particle morphology is another important property that affects particle ACN. Particle aspect ratio and its effect on the evolution of particle ACN was also studied. Fig. 20 summarizes the evolution of the ACN for all 10 triaxial specimens, in which particles that had a higher aspect ratio had a higher initial ACN and a higher ACN as the compression progressed. The rate of change of ACN was similar for all particles, and it seems that the aspect ratio of the particles did not change the rate of change of ACN. The dense specimens tested at high confining pressure ($\sigma_3 = 400$ kPa) had an initial rate of change of 0.04–0.2, followed by a sudden decrease at a rate of 0.1–0.3. The decreasing rate diminished and approached 0 as the test progressed. The behavior of dense specimens at low confining pressure ($\sigma_3 = 15$ kPa) had a similar trend; however, the initial rate of change was smaller than that of the dense specimens at high confining pressure. The initial increasing rate was between 0.012 and

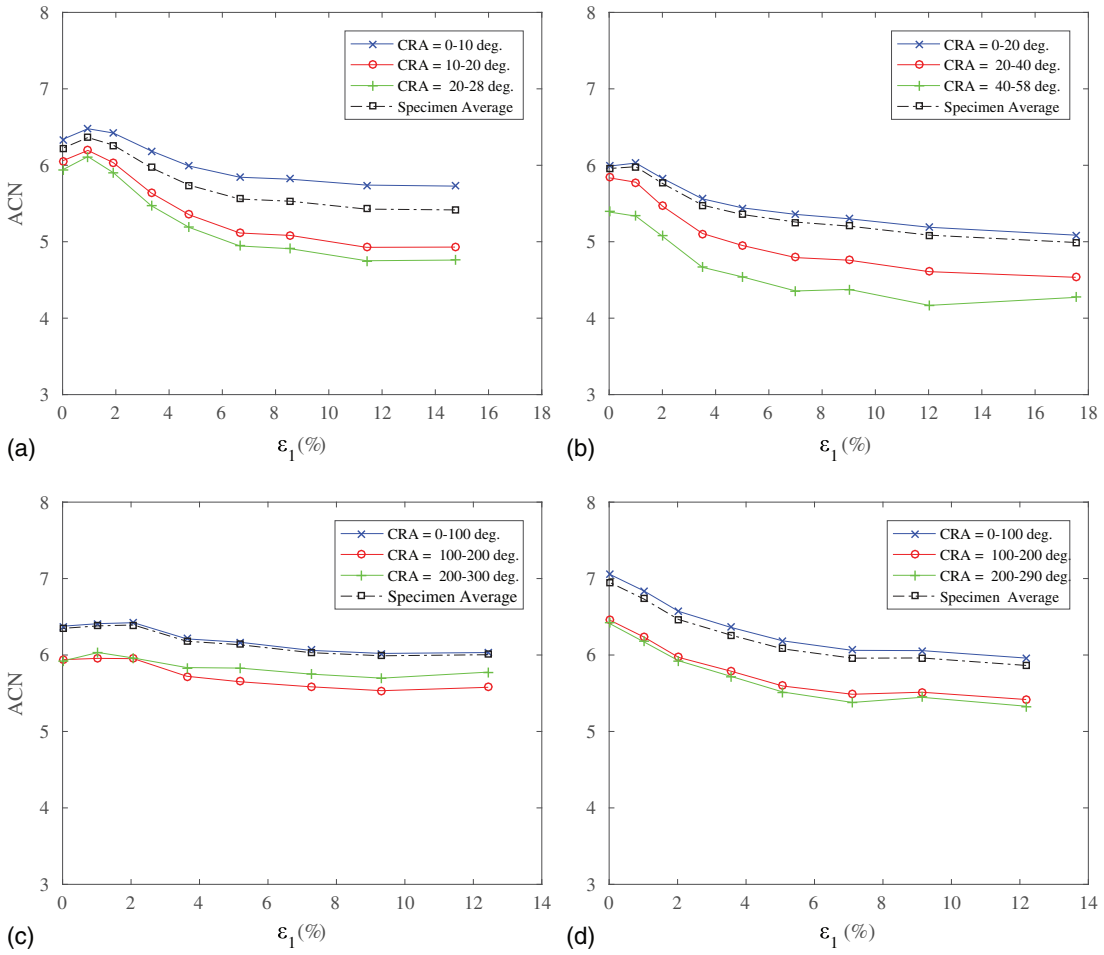

Fig. 19. (Color) Average contact number of GB and GS40 specimens: (a) GS40-D-400 kPa experiment; (b) GS40-D-15 kPa experiment; (c) GB-D-400 kPa experiment; and (d) GB-D-15 kPa experiment.

J. Geotech. Geoenviron. Eng., 2019, 145(2): 04018104

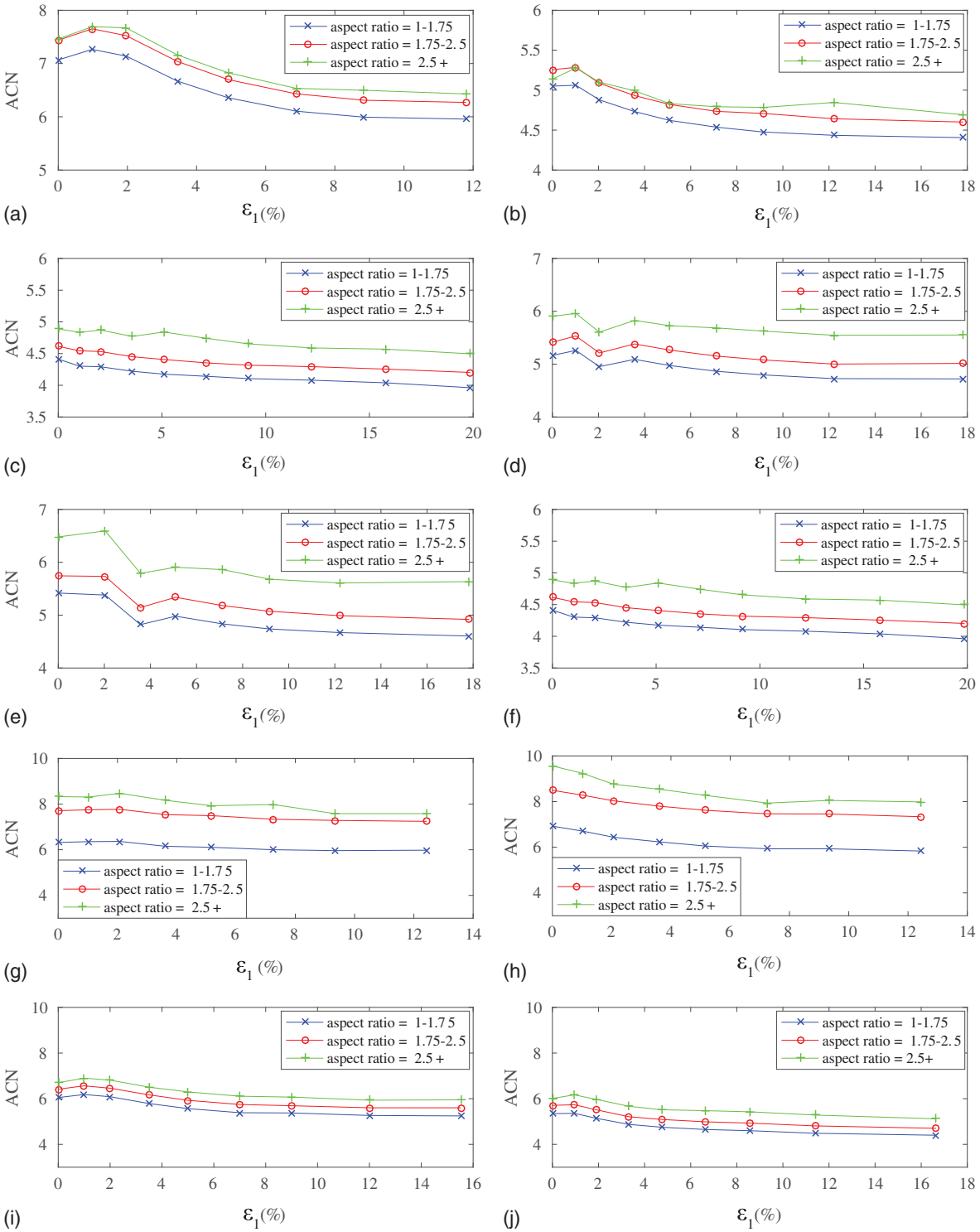

Fig. 20. (Color) Influence of particle aspect ratio on average contact number: (a) F35-D-400 kPa experiment; (b) F35-D-15 kPa experiment; (c) F35-L-15 kPa experiment; (d) DG-D-400 kPa experiment; (e) DG-D-15 kPa experiment; (f) DG-L-15 kPa experiment; (g) GB-D-400 kPa experiment; (h) GB-D-15 kPa experiment; (i) GS-D-400 kPa experiment; and (j) GS-L-15 kPa experiment.

0.025, followed by a sudden decrease at a rate between 0.17 and 0.25. The ACN approached a constant value during the final stage of the experiment. The loose specimens at low confining pressure ($\sigma_3 = 15$ kPa) exhibited a general decrease in the ACN during the test. The ACN initialy decreased at a rate of 0.05–0.08, and as the test progressed this rate approached values close to zero. Ting et al. (1995) and Ng (2004) investigated the effects of the aspect ratio of 2D and 3D particles using DEM and showed that particles with higher aspect ratios have a higher CN and less rotation. The elongation of a particle is expected to affect its tendency to rotate. The GB specimens did not have as many particles with aspect ratios higher than 2.5 due to their spherical shape.

J. Geotech. Geoenviron. Eng., 2019, 145(2): 04018104

Conclusions

SMT images were used to quantify kinematic behaviors of uniform sand and glass-bead specimens. The relative particle translation gradient concept of Druckrey et al. (2018) was adopted in this paper to expose the onset and evolution of micro shear bands that were otherwise undetectable using conventional cumulative or incremental particle translation and rotation. The following conclusions are drawn from the results reported in this paper.

The relative translation gradient of particles can expose intricate strain localizations better than conventional particle kinematics (cumulative or incremental translation and/or rotation).

Micro shear bands developed within all specimens during the strain hardening phase before the peak principal stress ratio. The MSBs evolved into a well-defined major final shear band in some of very dense specimens that were tested at $\sigma_3 = 400$ kPa, whereas a more complex zone of intensive shearing developed in medium-dense specimens and very dense specimens that were tested at $\sigma_3 = 15$ kPa.

Particle morphology influences the thickness and delineation of MSBs and the final major shear band. Particle roundness is the main contributor to particle interlocking, relative particle translation, and specimen tendency to develop a shear band.

Confining pressure influences the thickness and delineation of MSBs. MSBs that develop during strain hardening are more structured and better defined when a specimen is tested at a high confining pressure.

Particles with a higher initial ACN exhibit smaller rotation angles. Rotation causes contacts to form and break, and particles with a higher rotation have a higher variation in ACN than particles with smaller rotation angles.

Particles with a higher aspect ratio have a higher initial average contact number. At high strains, some of these ACN merged; however, particles with a higher aspect ratio still had a higher ACN. The change in ACN for particles with higher aspect ratio values was larger than for particles with smaller aspect ratio values.

Specimen density affects the rate of change of ACN. More contacts are broken than are newly formed, and the average CN decreased for very dense specimens, whereas newly formed contacts and broken contacts balance each other in medium-dense specimens, and smaller changes are visible in ACN. The specimen averages for both specimens approached each other at high strains, demonstrating that a critical state was reached.

Confining pressure has a similar effect as does specimen density: a higher confining pressure (except for glass beads) causes a higher initial ACN. As the compression progressed, the ACNs for both cases approached each other.

Acknowledgments

The research is funded by the US National Science Foundation (NSF) under Grant Nos. CMMI-1266230 and CMMI-1362510. Any opinions, findings, and conclusions or recommendations expressed in this paper are those of the authors and do not necessarily reflect the views of the NSF. The SMT images presented in this paper were collected using the X-Ray Operations and Research Beamline Station 13-BMD at Argonne Photon Source (APS), a US Department of Energy (DOE) Office of Science User Facility operated for the DOE Office of Science by Argonne National Laboratory under Contract No. DE-AC02-06CH11357. The authors acknowledge the support of GeoSoilEnviroCARS (Sector 13), which is supported by NSF–Earth Sciences (EAR-1128799), and DOE, Geosciences (DE-FG02-94ER14466). The authors thank Dr. Mark Rivers of APS for help performing the SMT scans.

References

Alshibli, K., A. Druckrey, R. Al-Raoush, T. Weiskittel, and N. Lavrik. 2014. "Quantifying morphology of sands using 3D imaging." *J. Mater. Civ. Eng.* 27 (10): 04014275. https://doi.org/10.1061/(ASCE)MT.1943-5533.0001246.

Alshibli, K., and L. Roussel. 2006. "Experimental investigation of slip-stick behaviour in granular materials." *Int. J. Numer. Anal. Methods Geomech.* 30 (14): 1391–1407. https://doi.org/10.1002/nag.517.

Alshibli, K. A., M. I. Alsaleh, and G. Z. Voyiadjis. 2006. "Modelling strain localization in granular materials using micropolar theory: Numerical implementation and verification." *Int. J. Numer. Anal. Methods Geomech.* 30 (15): 1525–1544. https://doi.org/10.1002/nag.534.

Alshibli, K. A., M. F. Jarrar, A. M. Druckrey, and R. I. Al-Raoush. 2017. "Influence of particle morphology on 3D kinematic behavior and strain localization of sheared sand." *J. Geotech. Geoenviron. Eng.* 143 (2): 04016097. https://doi.org/10.1061/(ASCE)GT.1943-5606.0001601.

Andò, E., S. Hall, G. Viggiani, J. Desrues, and P. Bésuelle. 2012a. "Experimental micromechanics: Grain-scale observation of sand deformation." *Géotech. Lett.* 2 (3): 107–112. https://doi.org/10.1680/geolett.12.00027.

Andò, E., S. A. Hall, G. Viggiani, J. Desrues, and P. Bésuelle. 2012b. "Grain-scale experimental investigation of localised deformation in sand: A discrete particle tracking approach." *Acta Geotechnica* 7 (1): 1–13. https://doi.org/10.1007/s11440-011-0151-6.

Batiste, S. N., K. A. AlshibliS. Sture, and M. Lankton. 2004. "Shear band characterization of triaxial sand specimens using computed tomography." *ASTM Geotech. Test. J.* 27 (6): 568–579. http://dx.doi.org/10.1520/GTJ12080.

Bouil, A., A. Amon, J.-C. Sangleboeuf, H. Orain, P. Bésuelle, G. Viggiani, P. Chasle, and J. Crassous. 2014. "A biaxial apparatus for the study of heterogeneous and intermittent strains in granular materials." *Granular Matter* 16 (1): 1–8. https://doi.org/10.1007/s10035-013-0477-x.

Desrues, J., and E. Andò. 2015. "Strain localisation in granular media." *C.R. Phys.* 16 (1): 26–36. https://doi.org/10.1016/j.crhy.2015.01.001.

Druckrey, A., and K. Alshibli. 2014. "3D behavior of sand particles using X-ray synchrotron micro-tomography." In *Proc., 2014 Geo-Congress—Geo-Characterization and Modeling for Sustainability, GSP 234*, 2814–2821. Atlanta: Geo-Institute of ASCE.

Druckrey, A., K. Alshibli, and R. Al-Raoush. 2018. "Discrete particle translation gradient concept to expose strain localisation in sheared granular materials using 3D experimental kinematic measurements." *Géotechnique* 68 (2): 162–170. https://doi.org/10.1680/jgeot.16.P.148.

Druckrey, A. M., K. A. Alshibli, and R. I. Al-Raoush. 2016. "3D characterization of sand particle-to-particle contact and morphology." *Comput. Geotech.* 74: 26–35. https://doi.org/10.1016/j.compgeo.2015.12.014.

Hall, S., M. Bornert, J. Desrues, Y. Pannier, N. Lenoir, G. Viggiani, and P. Bésuelle. 2010a. "Discrete and continuum analysis of localised deformation in sand using X-ray μCT and volumetric digital image correlation." *Géotechnique* 60 (5): 315–322. https://doi.org/10.1680/geot.2010.60.5.315.

Hall, S. A., D. Muir Wood, E. Ibraim, and G. Viggiani. 2010b. "Localised deformation patterning in 2D granular materials revealed by digital image correlation." *Granular Matter* 12 (1): 1–14. https://doi.org/10.1007/s10035-009-0155-1.

Hasan, A., and K. Alshibli. 2012. "Three dimensional fabric evolution of sheared sand." *Granular Matter* 14 (4): 469–482. https://doi.org/10.1007/s10035-012-0353-0.

Huang, W., K. Nübel, and E. Bauer. 2002. "Polar extension of a hypoplastic model for granular materials with shear localization." *Mech. Mater.* 34 (9): 563–576. https://doi.org/10.1016/S0167-6636(02)00163-1.

Jiang, M., H. Zhu, and X. Li. 2010. "Strain localization analyses of idealized sands in biaxial tests by distinct element method." *Front. Archit. Civ. Eng. China* 4 (2): 208–222. https://doi.org/10.1007/s11709-010-0025-2.

Kuhn, M. R. 1999. "Structured deformation in granular materials." *Mech. Mater.* 31 (6): 407–429. https://doi.org/10.1016/S0167-6636(99)00010-1.

Kuhn, M. R. 2003. "An experimental method for determining the effects of strain gradients in a granular material." *Commun. Numer. Methods Eng.* 19 (8): 573–580. https://doi.org/10.1002/cnm.613.

Kuhn, M. R., and K. Bagi. 2004. "Alternative definition of particle rolling in a granular assembly." *J. Eng. Mech.* 130 (7): 826–835. https://doi.org/10.1061/(ASCE)0733-9399(2004)130:7(826).

Mirghasemi, A., L. Rothenburg, and E. Matyas. 1997. "Numerical simulations of assemblies of two-dimensional polygon-shaped particles and effects of confining pressure on shear strength." *Soils Found.* 37 (3): 43–52. https://doi.org/10.3208/sandf.37.3_43.

Ng, T.-T. 2004. "Triaxial test simulations with discrete element method and hydrostatic boundaries." *J. Eng. Mech.* 130 (10): 1188–1194. https://doi.org/10.1061/(ASCE)0733-9399(2004)130:10(1188).

Oda, M., and K. Iwashita. 2000. "Study on couple stress and shear band development in granular media based on numerical simulation analyses." *Int. J. Eng. Sci.* 38 (15): 1713–1740. https://doi.org/10.1016/S0020-7225(99)00132-9.

Oda, M., K. Iwashita, and T. Kakiuchi. 1997. "Importance of particle rotation in the mechanics of granular materials." In Vol. 97 of *Powders grains*, edited by R. P. Behringer and J. T. Jenkins, 207–210. Rotterdam, Netherlands: A.A. Balkema.

Pena, A., R. Garcia-Rojo, and H. J. Herrmann. 2007. "Influence of particle shape on sheared dense granular media." *Granular Matter* 9 (3–4): 279–291. https://doi.org/10.1007/s10035-007-0038-2.

Rechenmacher, A. L. 2006. "Grain-scale processes governing shear band initiation and evolution in sands." *J. Mech. Phys. Solids* 54 (1): 22–45. https://doi.org/10.1016/j.jmps.2005.08.009.

Rechenmacher, A. L., and R. J. Finno. 2003. "Digital image correlation to evaluate shear banding in dilative sands." *Geotech. Test. J.* 27 (1): 13–22. https://doi.org/10.1520/GTJ11263J.

Rivers, M. L. 2012. "tomoRecon: High-speed tomography reconstruction on workstations using multi-threading." In Vol. 8506 of *Proc., Developments in X-Ray Tomography VIII*, 85060U. Washington, DC: International Society for Optics and Photonics.

Rivers, M. L., D. T. Citron, and Y. Wang. 2010. "Recent developments in computed tomography at GSECARS." In Vol. 7804 of *Proc., Developments in X-Ray Tomography VII*, 780409. Washington, DC: International Society for Optics and Photonics.

Rothenburg, L., and N. Kruyt. 2004. "Critical state and evolution of coordination number in simulated granular materials." *Int. J. Solids Struct.* 41 (21): 5763–5774. https://doi.org/10.1016/j.ijsolstr.2004.06.001.

Ting, J. M., L. Meachum, and J. D. Rowell. 1995. "Effect of particle shape on the strength and deformation mechanisms of ellipse-shaped granular assemblages." *Eng. Comput.* 12 (2): 99–108. https://doi.org/10.1108/02644409510799497.

Walker, D. M., A. Tordesillas, and A. L. Rechenmacher. 2013. "Transmission of kinematic information in dense granular systems: Local and nonlocal network sensing." *Acta Geotech.* 8 (5): 547–560. https://doi.org/10.1007/s11440-013-0266-z.